

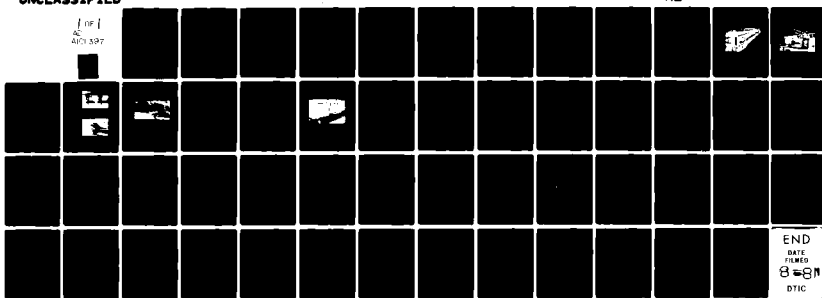
AD-A101 397

SOIL CONSERVATION SERVICE OXFORD MS SEDIMENTATION LAB F/6 20/4
STREAM CHANNEL STABILITY, APPENDIX L. STOCHASTIC PROPERTIES OF —ETC(U)
APR 81 C V ALONSO, N L COLEMAN

UNCLASSIFIED

NL

1 of 1
401 397



END
DATE
SERIAL
8-81
DTIC

AD A101397

LEVEL III

1

STREAM CHANNEL STABILITY

APPENDIX L

STOCHASTIC PROPERTIES OF TURBULENT TRACTIVE FORCES IN PRISMATIC CHANNELS

Project Objective 4

by

C. V. Alonso and N. L. Coleman

*USDA Sedimentation Laboratory
Oxford, Mississippi*

April 1981

DO NOT REPRODUCE
THIS DOCUMENT AND MAKE ITS
DISSEMINATION UNCONTROLLED.

*Prepared for
US Army Corps of Engineers, Vicksburg District
Vicksburg, Mississippi*

*Under
Section 32 Program, Work Unit 7*

DMC FILE COPY

81 7 14 095

STREAM CHANNEL STABILITY

APPENDIX L

STOCHASTIC PROPERTIES OF TURBULENT TRACTIVE
FORCES IN PRISMATIC CHANNELS

Project Objective 4

by

Carlos V. Alonso and Neil L. Coleman

USDA Sedimentation Laboratory

Oxford, Mississippi

April 1981

11/521

Prepared for

US Army Corps of Engineers, Vicksburg District
Vicksburg, Mississippi

Under

Section 32 Program, Work Unit 7

- 1/ Research Hydraulic Engineer, Sediment Transport and Deposition Research Unit, USDA Sedimentation Laboratory, Oxford, MS.
- 2/ Geologist; Research Leader, Sediment Transport and Deposition Research Unit, USDA Sedimentation Laboratory, Oxford, MS.

421-431

17

↓
PREFACE

The objective of this study is to develop a better understanding of the stochastic structure of the instantaneous boundary shear processes in open channel flows. This report presents new measurements of some stochastic properties of boundary shear stress taken at points spaced over half the wetted perimeter of a smooth open channel, under conditions of essentially constant aspect ratio and Reynolds number. The instantaneous boundary shear stress was measured with hot-film sensors driven by constant-temperature anemometers. The anemometer signals were digitized and analysed in a high speed computer. The effects of position along the wetted perimeter on the statistical moments and the probabilistic distribution of the instantaneous boundary shear stress are discussed.

↑

Accession For	
NTIS GR&I	
DTIC TAB	
Unannounced	
Justification	
<i>Refarm 50</i>	
By <i>on file</i>	
Distribution	
Availability Codes	
DTIC and/or	
Dist Specia	
A	

TABLE OF CONTENTS

List of Tables	3
List of Figures	4
U. S. Customary to S. I. Units Conversion Factors	5
1 Introduction	6
2 Experimental Arrangements and Procedures	8
2.1 The Flume System	8
2.2 The Boundary Shear Measuring System	11
2.3 Anemometry Equipment	11
2.4 Hot-Film Sensor Calibration	11
2.5 Flume Preparation and Data Collection	21
2.6 Discrete Data Processing	23
3 Presentation and Discussion of Results	28
3.1 General Flow Conditions	28
3.2 Statistical Descriptors	28
3.3 Probability Density Estimates	35
4 Conclusions and Recommendations	48
4.1 Conclusions	48
4.2 Recommendations	48
References	50

LIST OF TABLES

Table

1. Summary of hydraulic flow conditions	30
2. Summary of MLE parameters and Kolmogorov-Smirnov statistics	47

LIST OF FIGURES

Figure

1. View of the flume used in the tractive force experiments 9
2. View of multi-tube differential manometer and electronic measuring instruments 10
3. View of sliding probe support 12
4. View of rotating probe support 12
5. View of the measuring reach 13
6. Effect of sensor position relative to flow boundary 15
7. View of hot-film sensor mounted in calibration pipe 16
8. Configuration of the flush-mounted sensor 19
9. Variation of sensor response with azimuthal angle 20
10. Calibration for the boundary shear stress sensor 22
11. Diagram of electronic instruments and data flow path 24
12. Definition sketch for measuring point position 29
13. The ratio $\sigma_t/\bar{\tau}_0$ plotted against $2z/B$ for channel bed measurements .. 31
14. The ratio $\sigma_t/\bar{\tau}_0$ plotted against y/H for channel wall measurements .. 32
15. The variation of shear distribution skewness across the channel bed 33
16. The variation of shear distribution skewness up the channel wall .. 34
17. The variation of shear distribution kurtosis across the channel bed 36
18. The variation of shear distribution kurtosis up the channel bed 37
19. Observed probability density estimates for bed shear stresses at $2z/B=0.000$ (Run S-007) 41
20. Observed probability density estimates for bed shear stresses at $2z/B=0.510$ (Run S-032) 42
21. Observed and theoretical gamma probability density estimates for bed shear stresses at $2z/B=0.894$ (Run S-003) 43
22. Observed and theoretical gamma probability density estimates for wall shear stresses at $y/H=0.201$ (Run S-043) 44
23. Observed probability density estimates for wall shear stresses at $y/H=0.599$ (Run S-039) 45
24. Observed probability density estimates for wall shear stresses at $y/H=0.987$ (Run S-047) 46

U.S. Customary to S.I.-Units Conversion Factors

To convert	To	Multiply by
inches (in.)	millimeters (mm)	25.4
feet (ft)	meters (m)	0.305
yards (yd)	meters (m)	0.914
miles (miles)	kilometers (km)	1.61
square inches (sq. in.)	square millimeters (mm ²)	645
square feet (sq ft)	square meters (m ²)	0.093
square yards (sq yd)	square meters (m ²)	0.836
square miles (sq miles)	square kilometers (km ²)	2.59
acres (acre)	hectares (ha)	0.405
cubic inches (cu in.)	cubic millimeters (mm ³)	16,400
cubic feet (cu ft)	cubic meters (m ³)	0.028
cubic yards (cu yd)	cubic meters (m ³)	0.765
pounds (lb) mass	kilograms (kg)	0.453
tons (ton) mass	kilograms (kg)	907
pound force (lbf)	newtons (N)	4.45
kilogram force (kgf)	newtons (N)	9.81
pounds per square foot (psf)	pascals (Pa)	47.9
pounds per square inch (psi)	kilopascals (kPa)	6.89
U.S. gallons (gal)	liters (L)	3.79
acre-feet (acre-ft)	cubic meters (m ³)	1,233

INTRODUCTION

The beds of streams are composed of aggregates, the component particles of which can range in size from boulders and cobbles down to silt and clay. These streambed particles experience forces that are exerted on them by flowing water, and which tend to set them in motion, thus disturbing the stability of the streambed. This is the source of erosion in natural channels, and of damage to canals and irrigation ditches. Knowledge of those forces acting on the streambed is essential for the proper design of a stable channel cross section. It was thought for several years (White, 1940; Kalinske, 1943) that turbulent velocity fluctuations produce intermittent periods of high boundary shear stress, during which most sediment motion is initiated. Vanoni (1964) established by flume experiments that such fluctuations in shear stress do, indeed, produce intermittent episodes of bed material movement. He related this effect to the quasiperiodic disruptions of the viscous sublayer, described by Einstein and Li (1956). In current terminology, these intermittent events are called manifestations of the bursting phenomenon (Offen and Kline, 1975). Grass (1970; 1971) convincingly demonstrated by flow-visualization experiments a direct causal relationship between the bursting phenomenon and the intermittent entrainment of sediment bed particles. Raudkivi (1963) observed that entrainment of bed material can take place at values of time-averaged shear stress well below the value of critical stress defined by Shields' function. This observation can also be interpreted to indicate that different entrainment rates can be expected for bed shear stress distributions with different variances but equal mean values.

In spite of the foregoing facts, all the existing tractive-force models for the initiation of sediment motion have been based on the estimation of the time-average boundary shear stress distribution, and little progress has been made toward a sediment entrainment model incorporating stochastic properties of boundary shear stress. This is mostly due to the scarcity of adequate data on which to base the models. Some statistical properties of the turbulent hydrodynamic forces acting on discrete roughness elements were reported by Einstein and El-Samni (1949) and later on by Cheng and Clyde (1971). More recently, Blinco (1974) studied the fluctuation of the instantaneous boundary shear stress measured

on the centerline of a smooth open channel. He found that the characteristics of the shear stress fluctuation were Reynolds-number dependent.

Blinco's study was restricted to measurements of the bed centerline of a smooth open channel with an average aspect ratio of 5 and a systematic variation of Reynolds number. This report presents new measurements of some stochastic properties of boundary shear stress taken at points spaced over half the wetted perimeter of a smooth open channel, under conditions of essentially constant aspect ratio and Reynolds number. The effects of position along the wetted perimeter on the statistical moments and the probabilistic distribution of the instantaneous boundary shear stress are discussed. Part of the material presented in this report has been included in an earlier paper (Wylie et. al., 1977).

EXPERIMENTAL ARRANGEMENTS AND PROCEDURES

2.1 THE FLUME SYSTEM

Experiments were conducted in a recirculating flume 60 feet in length with a channel 1.969-feet wide and four-inches deep as shown in Fig. 1. The side walls, floor, pipeline, and all other parts of the flume in contact with the water are constructed of stainless steel, except for two 9.84-foot long plexiglass windows starting 32 feet below the channel entrance. The use of stainless steel avoids problems associated with corrosion and insures nearly hydraulically smooth boundary conditions. A centrifugal pump recirculates the water through a 4-inch return pipe located beneath the flume support structure. The flow is measured by a Venturi meter in the return line. The Venturi meter is connected to a mercury differential manometer that can be read to the nearest 0.1 inch. The meter was calibrated prior to this investigation and that calibration was used to determine the flume discharge. The flume is mounted on a central bearing pedestal and four interconnected motorized jacks, which provide a system for adjusting the flume slope. This is continuously adjustable from zero to 0.0200 and is set up by a mechanical counter previously calibrated to the slope. Water surface slope in the flume is measured using ten piezometer taps, evenly spaced along the flume, which are connected to a multiple-tube differential manometer (Fig. 2). The tubes of this manometer are separated by one-48th of the distance between the flume taps, and can be inclined simultaneously at varying angles. With this device the difference between piezometric head at successive taps can be magnified up to 250 times for accurate measurement of the water surface slope. An adjustable weir was located at the channel outlet to control the water surface elevation upstream. The water depth was measured directly by a point gauge suspended from a movable instrument carriage running on rails mounted on the channel walls. The ambient temperature around the flume was controlled and did not vary significantly during runs. An automatic heating element was installed in the flume tail tank, and the water maintained at a nearly constant temperature slightly above the ambient. Flow straighteners and a series of wire screens were installed at the entrance of the channel to eliminate large-scale turbulence disturbances and secondary flows. The measuring reach began 36 feet below the flume entrance, to insure that all measurements were made in the region of fully developed uniform flow.

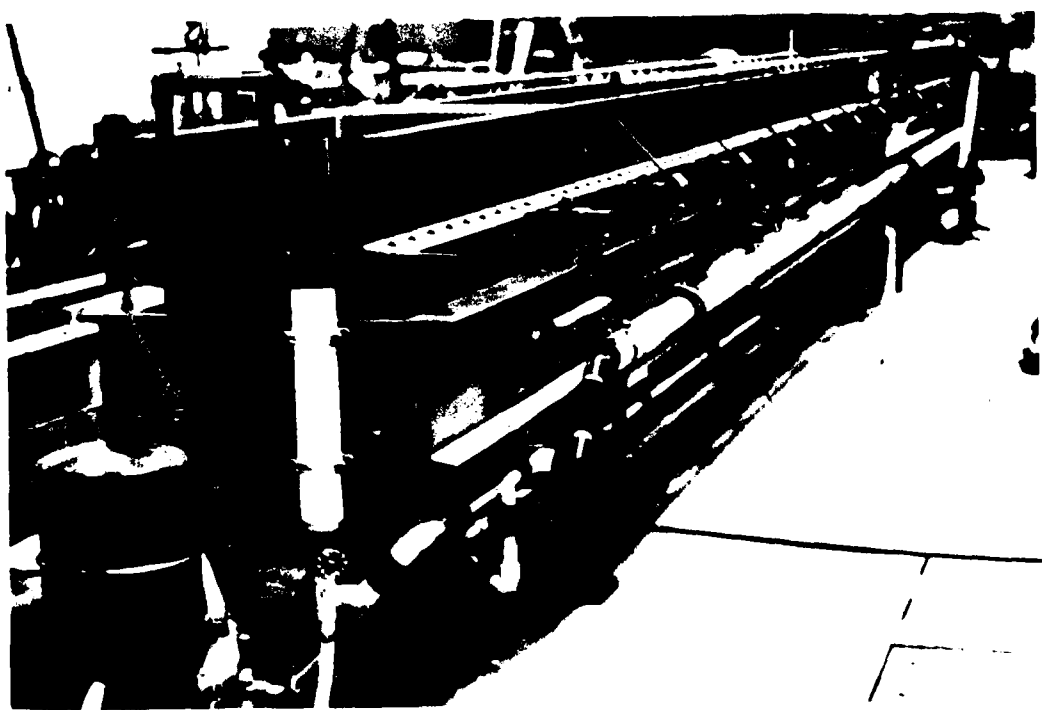


Fig. 1. View of the flume used in the tractive force experiments.

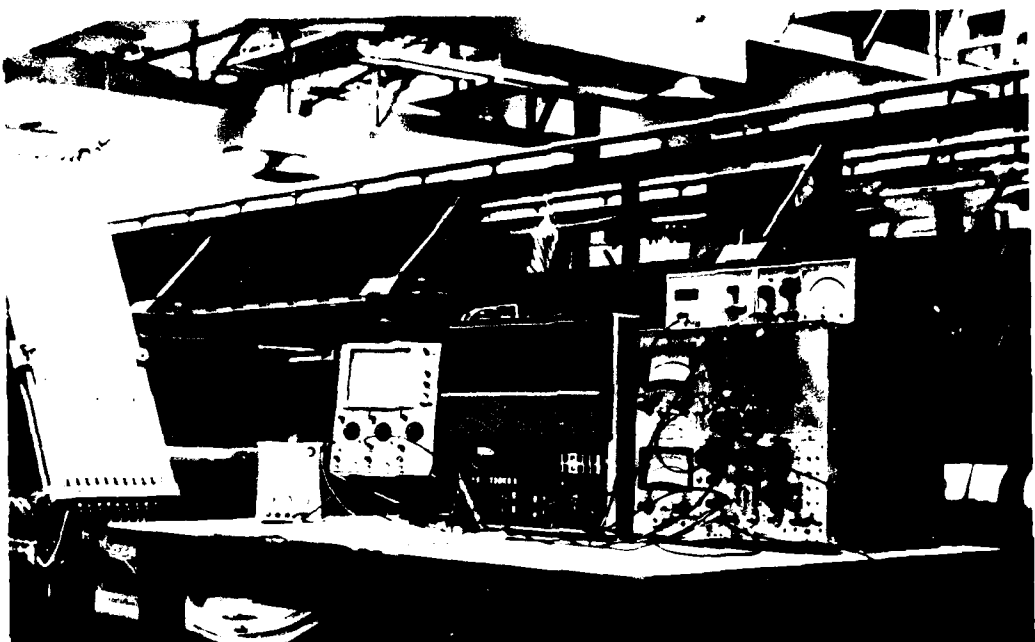


Fig. 2. View of multi-tube differential manometer and electronic measuring instruments.

2.2 THE BOUNDARY SHEAR MEASURING SYSTEM

Boundary shear stress was measured with a commercially available flush mounted hot-film sensor. Provisions were made to install the sensor in a series of holes drilled through the floor of the flume on a line from the flume centerline to the wall. A sliding block device, attached to the underside of the channel, permitted sensor positioning and movement along the flume floor with insignificant water loss (Fig. 3). This floor measuring section was located 38.4 ft. from the flume entrance. Sensor positioning along the flume wall was accomplished by a circular rotating block, attached to one of the plexiglass flume windows. A series of holes drilled through the window on a circular arc at predetermined heights above the channel bed, was mated with the sensor positioning hole in the rotating block (Fig. 4). This wall measuring section was located 36 ft. from the entrance of the flume channel. A discrepancy in the relative measuring locations was insignificant, since all positions were in uniform fully developed flow. Fig. 5 is a general view of that portion of the flume where measurements were taken.

2.3 ANEMOMETRY EQUIPMENT

The type of commercially available flush-mounted sensor used for boundary shear-stress measurements consisted of a platinum film, 1 mm long and 0.25 mm wide, electrically insulated by a thin layer of quartz. The major advantages of this type of sensor are that it does not disturb the flow, since its sensing face is actually part of the channel boundary, and that it measures shear stress at a point actually in the boundary itself.

The hot-film sensors were driven by a commercially available constant-temperature anemometer having an undistorted frequency response up to 5000 Hz. This system is a dual-channel unit, thus allowing two simultaneous measurements. During all experimental runs the anemometer signals were monitored on a dual channel oscilloscope for visual check on the signal integrities.

2.4 HOT-FILM SENSOR CALIBRATION

The flush mounted sensors used in this investigation were calibrated in a 46-ft by 4-inch plexiglass pipe, located on the same structural frame as the flume channel and connected in parallel with the flume return pipe

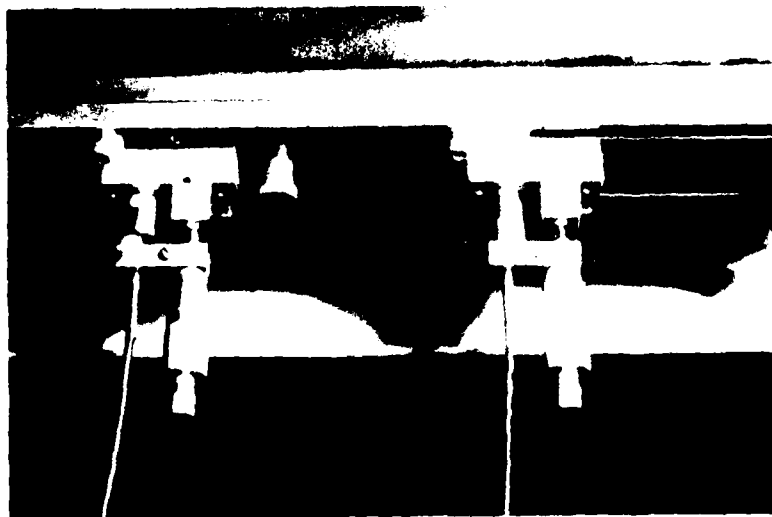


Fig. 3. View of sliding probe support.

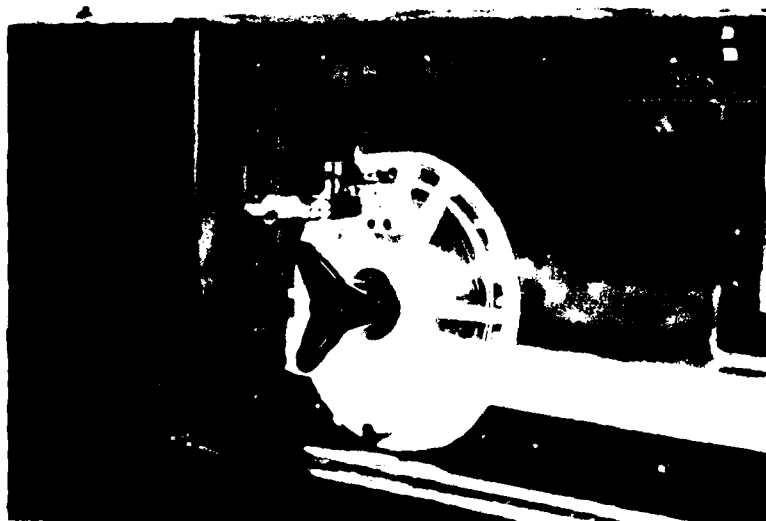


Fig. 4. View of rotating probe support.

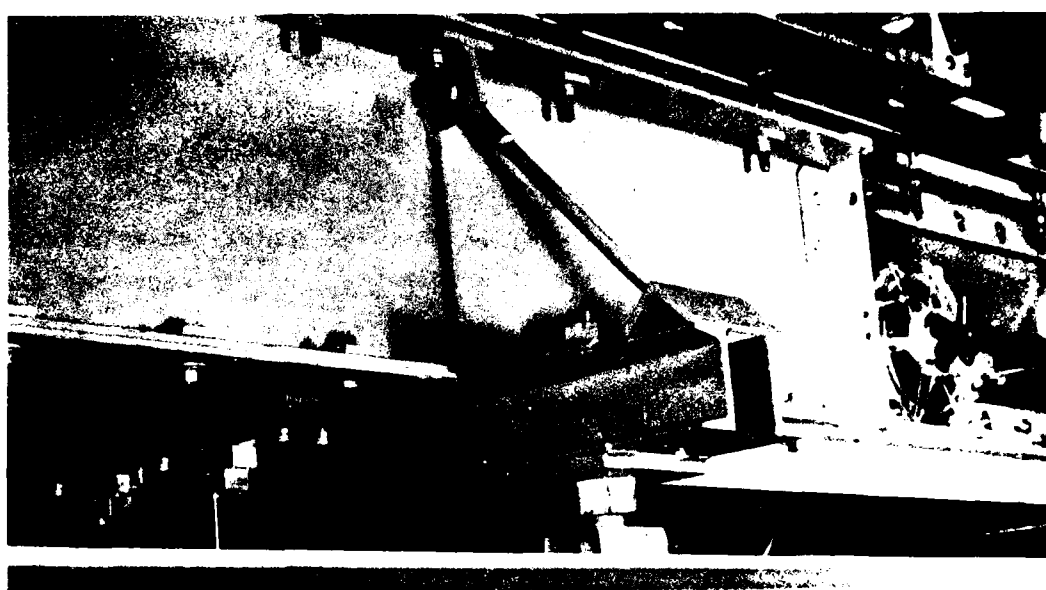


Fig. 5. View of the measuring reach.

(Fig. 1). A pipe was selected for the calibration because it has a cross-sectional shape for which the boundary shear stress is uniformly distributed. For fully developed pipe flow the boundary shear stress can be evaluated from the piezometric gradient. When the sensor was mounted flush on the pipe wall, it protruded about 0.0009 inch into the flow due to the curvature of the pipe wall. The minimum thickness of the pipe viscous sublayer encountered during calibration was of the order of 0.008 inch. Thus, the probe tip was fully submerged in the laminar sublayer, and it can therefore be assumed that the effects of any probe misalignment were negligible. This assumption was confirmed by preliminary tests conducted to evaluate the effect of sensor position in the mounting hole. This effect was studied by moving the sensor into and out of the flow at the ports in the calibration pipe and in the flume-floor centerline. As shown in Fig. 6, withdrawing the sensor from the hole very rapidly decreases the voltage output, indicating a smaller apparent shear stress value. Moving the sensor into the flow no more than about four thousandths of an inch results in a small voltage increase. Beyond this point the voltage increases rapidly indicating large apparent stresses. Therefore, it was concluded that very small projections of the sensor into the flow do not have an appreciable effect on the measurements.

The flush mounted sensor was placed in a mounting block located 95 diameters from the calibration pipe entrance. Piezometer taps spaced 48 inches apart along the pipe, and connected to the multiple-tube manometer mentioned earlier, allowed measurement of the piezometric head gradient. Fig. 7 shows a closeup photo of the sensor in the mounting block. After calibration, the sensor was carefully positioned flush with the floor, or wall, of the flume channel. During calibration the anemometer output was checked against the pipe-wall shear stress, $\bar{\tau}$, computed from

$$\bar{\tau} = \gamma \frac{D}{4} S_f , \quad (1)$$

where γ is the water specific weight, D is the pipe diameter, and S_f is the piezometric-head gradient along the pipe.

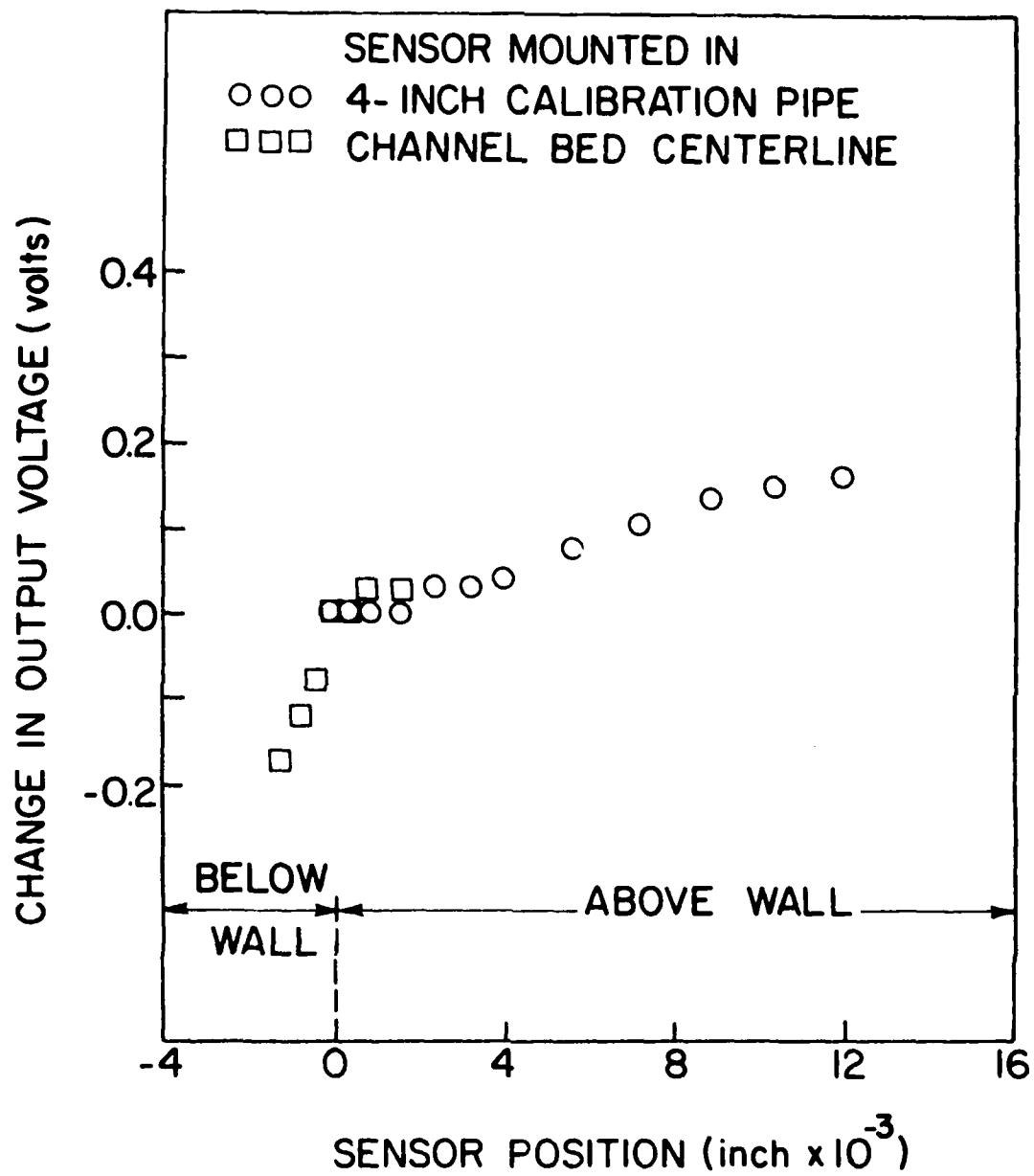


Fig. 6. Effect of sensor position relative to flow boundary.

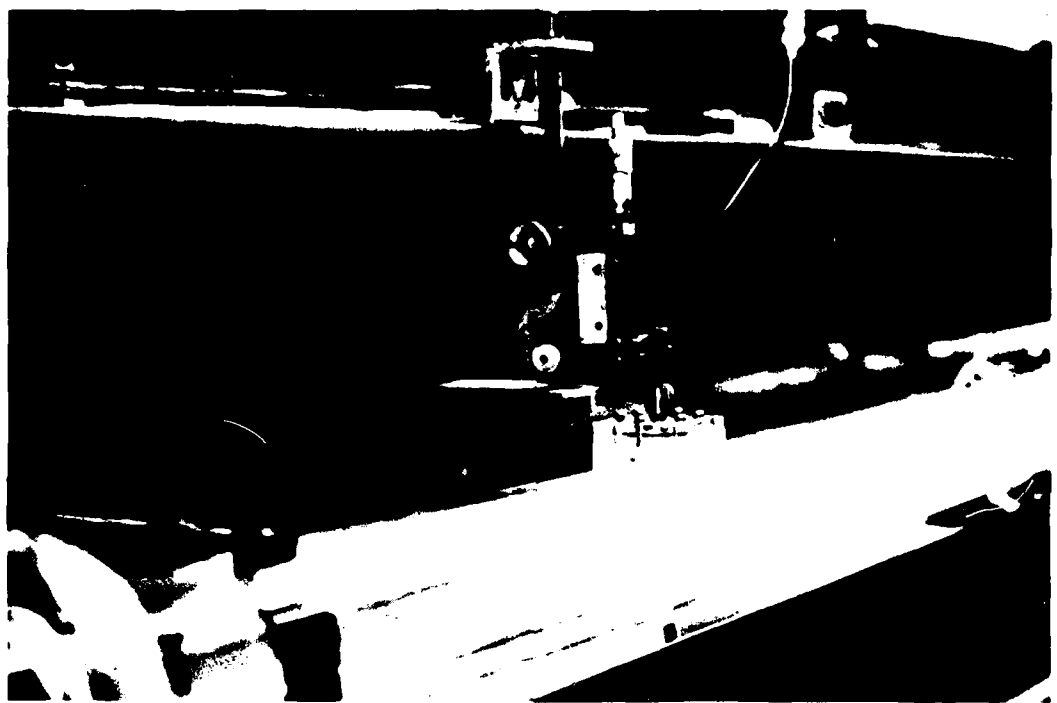


Fig. 7. View of hot-film sensor mounted in calibration pipe.

The relation of \bar{t} to the anemometer output is obtained from the following considerations. Curle (1962) and Bellhouse and Schultz (1966, 1967) studied a steady, two-dimensional viscous layer and showed that the heat flow equation of the boundary layer can be written as

$$\frac{d}{dx} \int_0^\infty \bar{u} (\theta - \theta_\infty) d\eta = - \frac{1}{\rho c_p} q_w(x) , \quad (2)$$

where x is the distance measured in the direction of mean fluid motion, η is the distance measured perpendicularly to the wall, u is the local mean velocity, θ is the fluid temperature at η , θ_∞ is the fluid temperature at $\eta \rightarrow \infty$, $q_w(x)$ is the heat flowing from the heated sensor to the fluid, ρ is the fluid density, and c_p is the specific heat of the fluid at constant pressure. Assuming that the thermal boundary layer thickness is smaller than the viscous sublayer thickness, and that the velocity distribution is given by

$$\bar{u} = \frac{\bar{t}\eta}{\mu} + \frac{1}{2\mu} \frac{dp}{dx} \eta^2 , \quad (3)$$

Eq. 2 can be expressed as

$$\frac{d}{dx} \int_0^\infty \bar{t}\eta (\theta - \theta_\infty) d\eta + \frac{1}{2} \frac{dp}{dx} \int_0^\infty \eta^2 (\theta - \theta_\infty) d\eta = - \frac{\mu^2}{\rho k P_r} q_w(x) , \quad (4)$$

in which \bar{p} is the mean ambient pressure, μ is the dynamic viscosity of the fluid, k is the fluid heat conductivity, and P_r is the Prandtl number of the fluid. Since the substratum of the sensor is sufficiently nonconductive, $q_w(x)$ and $\theta_w(x)$ can be regarded as step functions over the sensor effective length. Curle (1962) also assumed that the temperature profile would not vary appreciably over a moderate range of pressure gradients. Based on these assumptions Curle solved Eq. 4 to obtain the response of a flush-mounted sensor of length ℓ , and width, d , (Fig. 8) used as a constant temperature transducer. The result is

$$\bar{t}^{1/3} = - \frac{q_w \ell d}{k \Delta \theta_{ad}^{2/3}} (\rho/P_r)^{1/3} \quad (5)$$

where $\Delta\theta = \theta - \theta_\infty$ is the temperature difference between sensor and fluid, and a is a constant. Relating the electrical power, E^2/R , used in heating the element to the heat dissipated through the sensor surface, $q_w \ell d$, Eq. 5 can be written as

$$\frac{E^2}{R(R-R_0)} = A + B \tau_e^{1/n}, \quad (6)$$

where E is the instantaneous anemometer-bridge output voltage, R is the electrical resistance of the sensor at operating temperature, R_0 is the (cold) resistance of the sensor at ambient fluid temperature, A , B , and n are constants to be determined by calibration, and τ_e is the effective boundary shear stress on the channel boundary. This stress is defined by

$$\tau_e^2 = (\bar{\tau}_{\eta x} + \tau'_{\eta x})^2 + (\tau'_{\eta \zeta})^2, \quad (7)$$

where $\bar{\tau}_{\eta x}$ is the time mean stress acting in the x direction, due to mean viscous shear, and $\tau'_{\eta x}$, $\tau'_{\eta \zeta}$ are fluctuating stress components due to instantaneous viscous friction (Fig. 8). Past experience with turbulent open channel flows indicates that near the channel boundary transverse turbulent velocity fluctuations are considerably less than longitudinal fluctuations. Moreover, the hot-film sensor exhibits less thermal sensitivity to changes in transverse flow because of its greater size in that direction. Therefore, for moderate turbulence intensities, the sensor is essentially sensitive to viscous shearing in the mean flow direction. A series of measurements were performed to establish the limits of this assumption. The sensor was located at the centerline of the flume floor and perpendicular to the flow direction. The response of the sensor to azimuthal position was determined by rotating the sensor at five-degree increments and measuring the boundary shear stress. The results of this calibration are summarized in Fig. 9. It can be concluded that the sensor response is independent of the azimuthal angle as long as it does not deviate more than ten degrees from the perpendicular position.

Consequently, Eq. 6 can be written

$$\frac{E^2}{R(R-R_0)} \approx A + B (\bar{\tau}_{\eta x} + \tau'_{\eta x})^{1/n}. \quad (8)$$

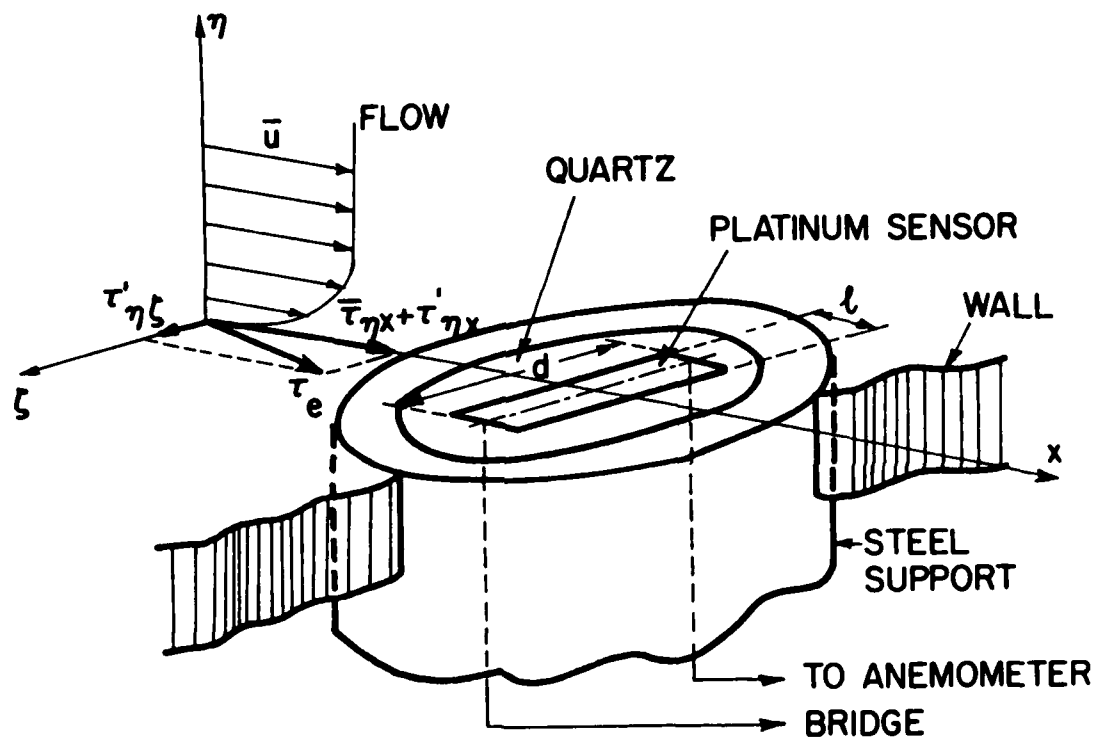


Fig. 8. Configuration of the flush-mounted sensor.

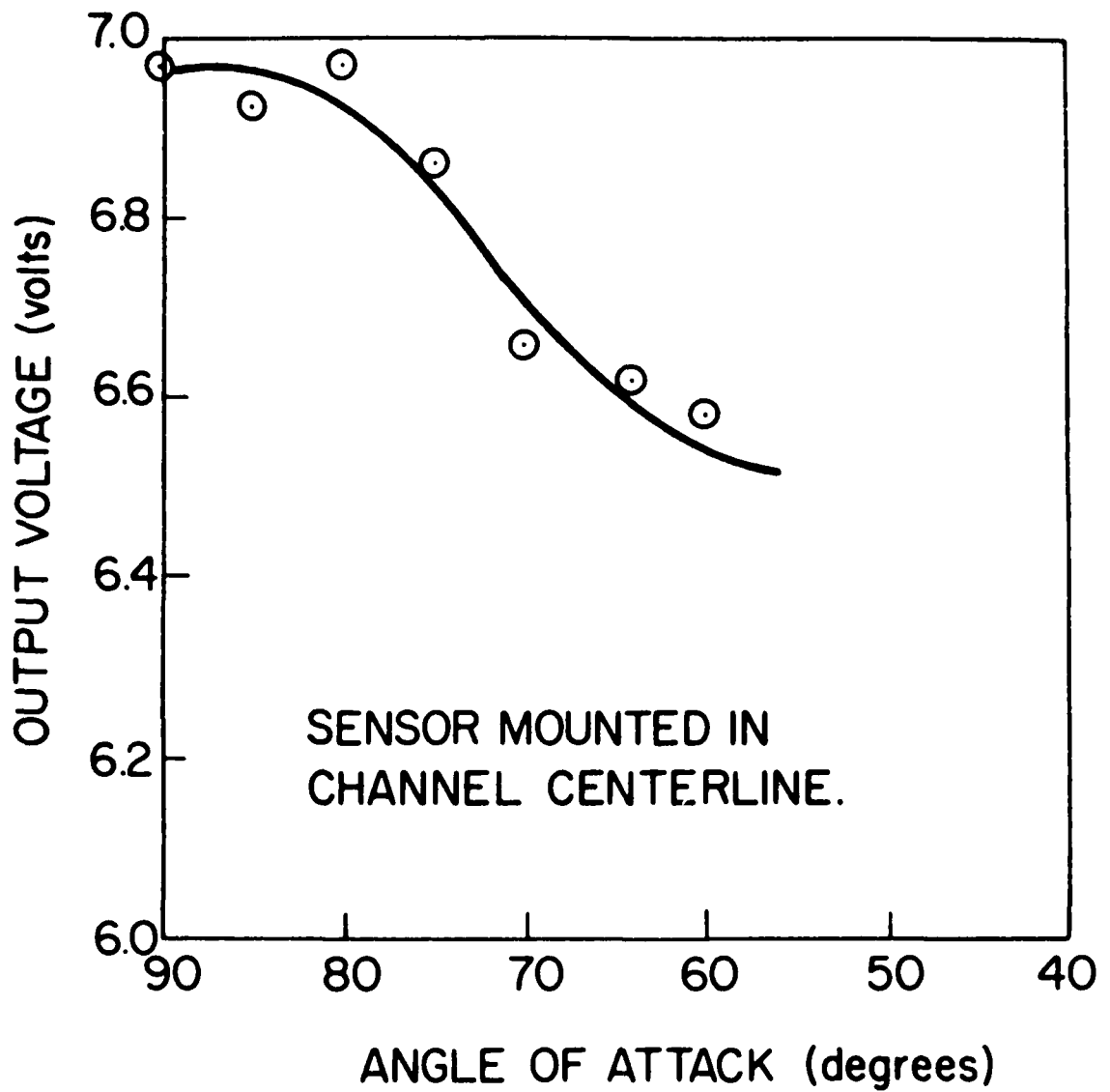


Fig. 9. Variation of sensor response with azimuthal angle.

Expanding the right hand side of this equation and time averaging yields the expression used in calibrating the sensor,

$$\frac{(\bar{E}/R_o)^2}{H_R(H_R-1)} = A + B \bar{\tau}_{\eta x}^{1/n}, \quad (9)$$

in which $H_R = R/R_o$ is the overheat ratio, and $\bar{\tau}_{\eta x}$ is given by Eq. 1. Regression analysis of measured output voltages and pipe wall shears was used to determine the calibration constants A, B, and n. Fig. 10 is a composite curve plotted from several calibrations over a six-month period. It shows good repeatability, and demonstrates that the flush-mounted sensor is very stable in maintaining its calibration. The slope of the calibration depends on the overheat ratio. This value was maintained at 1.05 in the present experiments to prevent formation of bubbles on the sensor.

Applicability of Eq. 8 is predicated on the existence of a thermal boundary layer thinner than the viscous sublayer. Therefore, a criterion is needed to determine when a particular flow satisfies that condition. Brown (1967) has developed a criterion by studying the response of a heated sensor where the wall temperature is not a simple step function. Based on experimental evidence Brown concluded that the wall temperature decays exponentially along the sensor length ℓ . By further assuming a linear velocity variation near the wall, he obtained a solution of the thermal energy equation which shows that Eq. 8 is a good approximation when the following inequality is satisfied,

$$\frac{u_* \ell}{v} < 64 \text{ Pr} \quad (10)$$

Here u_* is the wall shear velocity, and v is the fluid kinematic viscosity. The maximum shear velocity encountered in the present study was 0.091 fps and the minimum value of the Prandtl number was about $P_r = 6$, which shows that Brown's criterion was satisfied in all the experimental runs.

2.5 FLUME PREPARATION AND DATA COLLECTION

The flume pumping system was turned on well in advance of the start of an experiment to insure a uniform and stable distribution of temperature

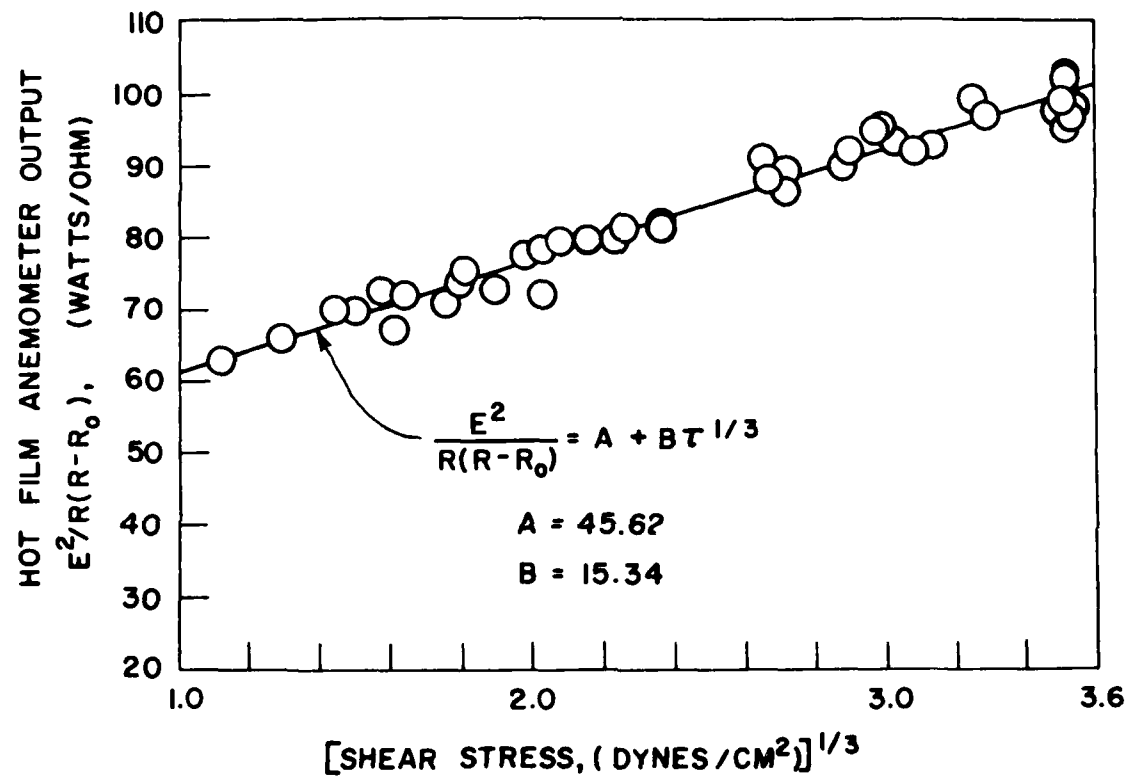


Fig. 10. Calibration for the boundary shear stress sensor.

throughout the water in the flume. During this period the discharge control, flume slope, and tail weir were adjusted until uniform flow was established for the desired depth and discharge. This was verified by comparing the flume slope to the water-surface slope measured with the multi-tube differential manometer. Assuming that the whole channel boundary layer from the entrance is turbulent, and using Prandtl's 4/5-law for the variation of the boundary-layer thickness, the following estimate of the location x_* at which the flow is fully developed is obtained

$$x_* \approx (H/0.38)^{5/4} (U/v)^{1/4} \quad (11)$$

where H is the flow depth, and U is the average flow velocity. Because the largest values of H and U used in this study yield $x_* \approx 24$ feet, the boundary layer was assumed fully developed over the measuring reach. The water temperature was continuously monitored to insure that it did not change more than $\pm 1^{\circ}\text{F}$ during a run. The precalibrated probe was installed in the centerline port in the flume floor, and then moved successively across the floor and up the flume wall as measurements were taken.

All measurements were made with the anemometer set so that frequency components above 500 Hz were filtered out. For each measurement, the direct current component of the anemometer bridge output was continuously measured with a DC voltmeter, and suppressed in the signal conditioning portion of the circuit. The remaining output from the signal conditioner was amplified ten times to improve the AC voltage signal to noise ratio. The amplified signal was recorded on a 4-channel FM analog tape to store the data as it was collected. Immediately afterwards, a sinusoidal signal of known amplitude and frequency was recorded on the same channel for subsequent calibration of the FM-tape output voltage. A flow chart depicting the instruments and data flow path is shown in Fig. 11. After the recordings were completed, the sensor was moved to the next position, and the whole process was repeated.

2.6 DISCRETE DATA PROCESSING

The analog instruments available during these measurements allowed only measurement of the mean and variance of the fluctuating signals. These parameters are statistical measures of the probability distribution of the fluctuations. However, knowing the probability distribution the

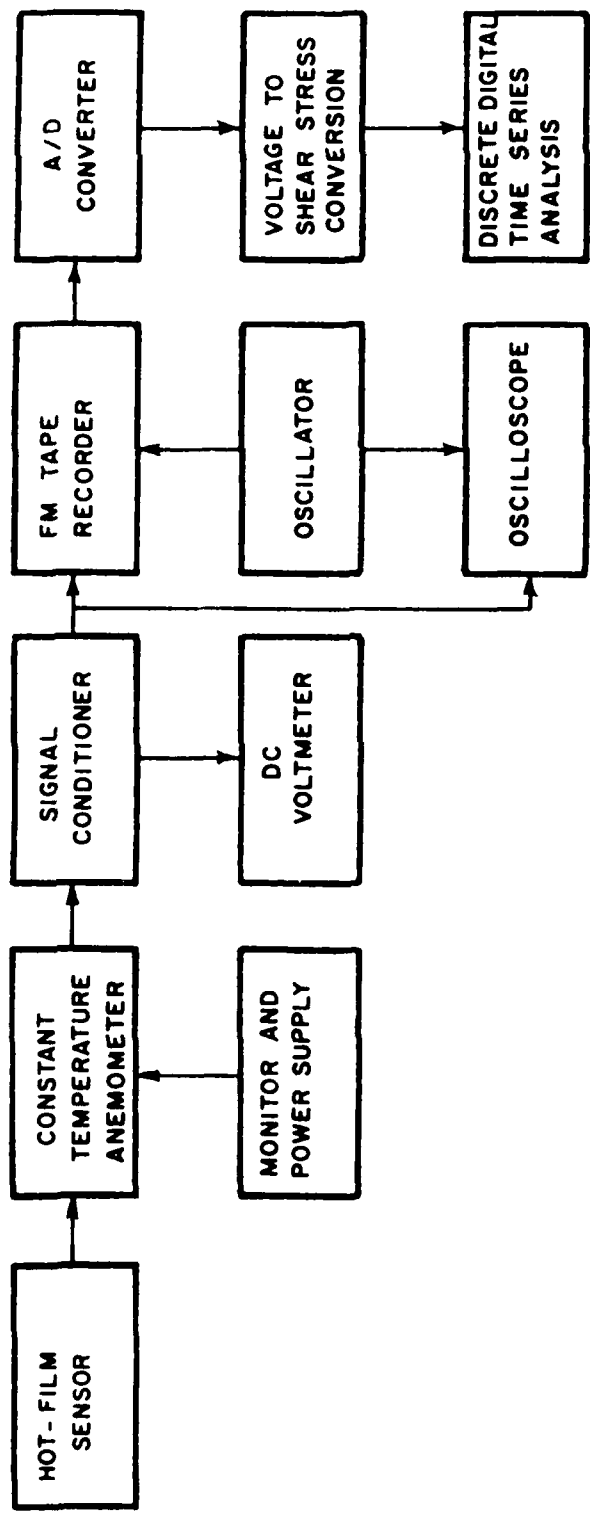


Fig. 11. Diagram of electronic instruments and data flow path.

statistical moments can be computed, whereas the mean and the variance do not completely describe the distribution function. To overcome this problem, it was decided to transform the analog output voltages into discrete boundary shear stresses using digital equipment available at the Sedimentation Laboratory. The discretized data was then processed to obtain the required statistics. The FM analog tape was played back into an analog-to-digital (A/D) converter. The A/D output was stored on computer compatible digital magnetic tape.

Before processing the analog data it was necessary to select the sampling rate and the record length. The sampling rate, or number of samples measured per second, should not be so high as to result in data points spaced too closely. This condition causes the data to be redundant. The minimum sampling rate that will contain all the information in a signal of given frequency is called the Nyquist frequency, f_N . This frequency is equal to twice the frequency of the signal being analyzed. If the sampling rate is less than twice the highest frequency component in the signal, aliasing can occur. In equally spaced data, two frequencies, f_1 and f_2 , are aliases of one another if sinusoids of the corresponding frequencies cannot be distinguished by their equally spaced values. This occurs when $f_1 = 2kf_N \pm f_2$, for $k=1, 2, 3, \dots$. Previous measurements of turbulent-velocity power spectra in water flowing over smooth walls indicate that most of the energy content is associated with frequencies less than 150 Hz (Alonso et. al., 1976). Allowing for a "safety zone" of 50 Hz, the frequency range expected to contain significant information is 0-200 Hz. This results in a Nyquist frequency of 400 Hz. Assuming that the instantaneous boundary shear stresses follow the fluctuations of the turbulent velocities near the wall, a sampling rate of 400 samples per second was selected, corresponding to the above Nyquist frequency. The analog data was recorded for about 5 minutes in all cases at the specified sampling rate. This gives a total record length of 120,000 data points. Less than this full length was used to determine the statistical moments and probability distributions in order to reduce the computation times. A subsample size was chosen by examining the variation of the sample mean and standard deviation with different record lengths. Based on this study, a subsample length of 30,000 points was selected. The sample mean and standard deviations for this record length did not vary significantly from those for the entire record length.

The digitized voltage values were converted to discrete shear stress values using a digital computer by first dividing each voltage by ten, the gain of the amplifier, then adding back the suppressed DC voltage, and finally, converting voltages to shear stress by means of Eq. 9. From the subsample of size $N=30,000$, the average shear stress, μ_τ ; variance, σ_τ^2 ; coefficient of skewness, S_τ ; and the kurtosis, K_τ , were computed from

$$\mu_\tau = \frac{1}{N} \sum_{i=1}^N \tau_i , \quad (12)$$

$$\sigma_\tau^2 = \frac{1}{N} \sum_{i=1}^N (\tau_i - \mu_\tau)^2 , \quad (13)$$

$$S_\tau = \frac{1}{N} \sum_{i=1}^N \left(\frac{\tau_i - \mu_\tau}{\sigma_\tau} \right)^3 , \quad (14)$$

$$K_\tau = \frac{1}{N} \sum_{i=1}^N \left(\frac{\tau_i - \mu_\tau}{\sigma_\tau} \right)^4 , \quad (15)$$

where τ_i indicates the instantaneous shear stress value at a point. Although these are biased estimates, the error was insignificantly small for the large number of data points in the sample record. The probability density estimates were determined using the following procedure. The data range $[a \leq \tau_i \leq b]$ was divided into K class intervals of width

$$c = \frac{b-a}{K} \quad (16)$$

where K is given by (Ottes and Erochson, 1972)

$$K = 1.87 (N-1)^{2/5} - 2. \quad (17)$$

The probability density estimate for the midpoint of each class interval was defined as

$$\hat{p}_j = \frac{1}{c} \text{Prob} [\tau_{j-c/2} < \tau_i \leq \tau_{j+c/2}], \quad j = 1, 2, \dots, K. \quad (18)$$

where $\text{Prob} [.] = N_j/N$, and N_j is the number of occurrences of τ_i in the j th class interval. To obtain the class frequencies, a value $L = (\tau_i - a)/c$ is computed for each stress value. The largest integer $j \leq L$ is found, and then

one is added to N_j . The maximum, b, and minimum, a, values of the stress data were obtained in all cases from preliminary analysis of the data records.

The individual shear stress values were standardized by subtracting the mean value and then dividing by the standard deviation of the sample, that is

$$\tau_i^* = (\tau_i - \mu_\tau) / \sigma_\tau . \quad (19)$$

Plotting the stress values in this standardized form helps to visualize the data range in terms of multiples of the standard deviation which, in turn, is a measure of the spread of the fluctuating stresses. The corresponding probability density estimates were derived from the requirement that the areas under the standardized and nonstandardized probability density functions be equal. Thus, for any class interval one has

$$\hat{p}_j^* \left(\frac{\tau_j - \mu_\tau}{\sigma_\tau} - \frac{\tau_{j-1} - \mu_\tau}{\sigma_\tau} \right) = \hat{p}_j c ,$$

or, $\hat{p}_j^* \frac{c}{\sigma_\tau} = \hat{p}_j c ,$

$$\text{and finally, } \hat{p}_j^* = \sigma_\tau \hat{p}_j . \quad (20)$$

PRESENTATION AND DISCUSSION OF RESULTS

3.1 GENERAL FLOW CONDITIONS

Figure 12 is a definition sketch for the positioning of measurement points on the flume floor and wall. The holes for sensor insertion were located at preselected values of the normalized positions $2z/B$ on the floor and y/H on the wall. Table 1 summarizes flow conditions for twenty-four measurements made at an aspect ratio of about 4.4 and a Reynolds number of about 1.7×10^5 . The aspect ratio was slightly lower than the average ratio of 5 used by Blinco (1974), whereas the Reynolds number was a little larger than the largest value used by Blinco. The Froude number in the table is defined as U/\sqrt{gH} and the Reynolds number as $4R_h U/v$, where R_h indicates the hydraulic radius of the flow. The average unit tractive forces listed in the table were calculated from the usual duBoys equation for open channels $\bar{\tau}_o = yR_h S_o$, in which S_o is the channel bed slope. The aspect ratio is defined conventionally as the ratio of flow width, B , to flow depth, H .

3.2 STATISTICAL DESCRIPTORS

As mentioned earlier, each run listed in Table 1 consisted of a record length of 30,000 digital shear-stress sample values, and the sample mean, standard deviation, skewness and kurtosis were computed for each run. In Fig. 13, the ratio $\sigma/\bar{\tau}_o$ of standard deviation to unit mean shear stress has been plotted against $2z/B$ for positions across the channel bed. The same ratio is plotted against y/H in Fig. 14 for positions up the wall. This ratio goes through a minimum at about $2z/B = 0.6$ on the bed and through a maximum at about $y/H = 0.4$ on the wall. The trends are similar to those exhibited by the ratio between the local mean shear and $\bar{\tau}_o$ for similar aspect ratios (Kartha and Leutheusser, 1970). This suggested that the standard deviation of fluctuating shear, as is the case for the mean shear, is affected by secondary circulation in the mean flow. Also, the $\sigma/\bar{\tau}_o$ trend along the bed resembled the distribution of relative turbulent intensities of longitudinal velocities measured very close to the wall of a square duct by Melling and Whitelaw (1973).

Figures 15 and 16 show the variations of skewness along the channel bed and walls, respectively. The coefficient of skewness is a measure of the asymmetry of a probability distribution and is zero for a normal distribution. In these measurements, the distributions were all positively skewed, and the variation of skewness along both bed and wall was quasi-periodic.

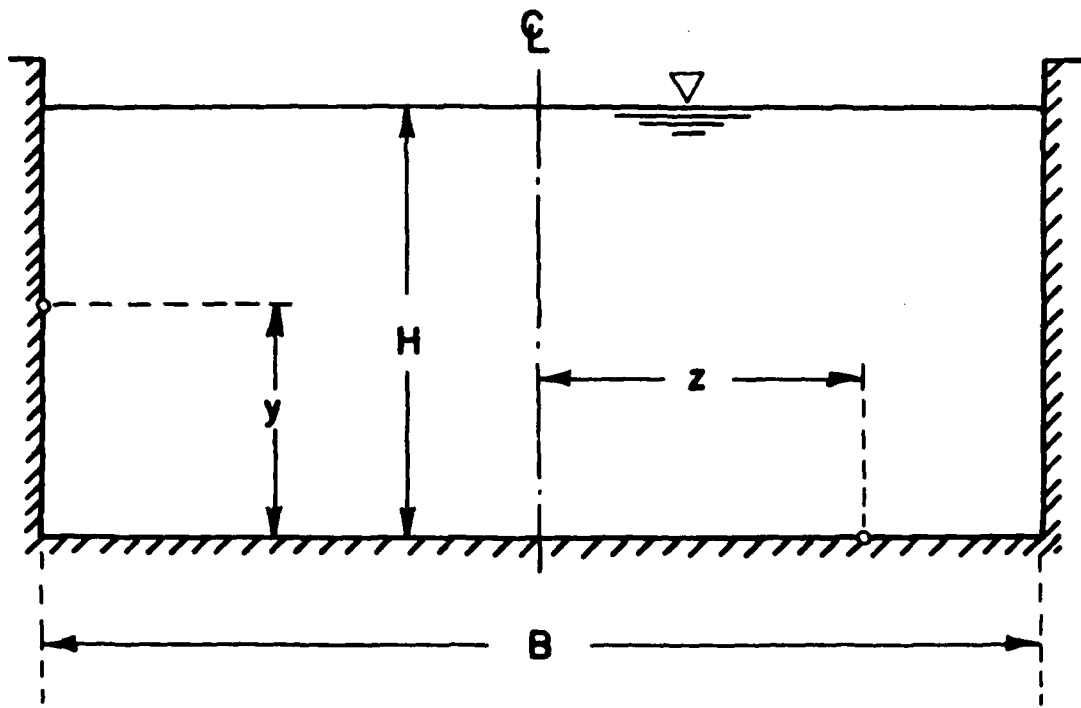


Fig. 12. Definition sketch for measuring point position.

Table 1 - Summary of hydraulic flow conditions

Run Number	Probe Location			Depth	Discharge	Temp.	Bed Slope $\times 10^3$	Reynolds Number $\times 10^{-5}$	Av. Unit		
	x m	y cm	z cm						Aspect Ratio	Froude Number	Tractive Force Number dynes/cm ²
S-036	10.72	2.2	29.8	13.7	0.0338	24.5	0.490	4.36	1.72	0.36	4.497
S-043	10.72	2.8	29.8	13.8	0.0339	22.6	0.556	4.32	1.64	0.35	5.137
S-037	10.72	3.4	29.8	13.7	0.0338	24.7	0.490	4.36	1.72	0.36	4.497
S-042	10.72	3.4	29.8	13.7	0.0338	24.7	0.490	4.36	1.72	0.36	4.497
S-044	10.72	4.1	29.8	13.8	0.0338	22.8	0.556	4.32	1.64	0.35	5.137
S-038	10.72	4.8	29.8	13.7	0.0338	24.9	0.490	4.37	1.74	0.36	4.490
S-045	10.72	6.3	29.8	13.8	0.0339	23.2	0.564	4.33	1.66	0.35	5.202
S-039	10.72	8.2	29.8	13.7	0.0338	25.0	0.490	4.37	1.74	0.36	4.490
S-046	10.72	9.7	29.8	13.7	0.0339	23.6	0.564	4.34	1.68	0.36	5.194
S-040	10.72	12.1	29.8	13.6	0.0339	25.0	0.490	4.38	1.74	0.36	4.483
S-047	10.72	13.6	29.8	13.7	0.0339	23.8	0.564	4.34	1.69	0.36	5.194
S-007	11.73	0.0	0.0	13.5	0.0338	23.7	0.500	4.41	1.69	0.36	4.555
S-035	11.73	0.0	0.0	13.7	0.0338	25.4	0.490	4.35	1.75	0.36	4.503
S-008/9	11.73	0.0	3.8	13.5	0.0338	24.2	0.500	4.41	1.70	0.36	4.551
S-010	11.73	0.0	7.6	13.5	0.0338	24.5	0.520	4.43	1.72	0.37	4.722
S-011	11.73	0.0	11.4	13.5	0.0338	24.6	0.520	4.42	1.73	0.36	4.729
S-012	11.73	0.0	15.2	13.5	0.0338	24.6	0.487	4.42	1.73	0.36	4.429
S-006	11.73	0.0	15.2	13.5	0.0338	23.4	0.500	4.41	1.68	0.36	4.555
S-048	11.73	0.0	19.0	13.8	0.0335	23.8	0.439	4.32	1.67	0.35	4.055
S-004	11.73	0.0	22.9	13.5	0.0338	21.9	0.369	4.42	1.62	0.36	3.358
S-033	11.73	0.0	22.9	13.4	0.0338	24.8	0.487	4.45	1.74	0.37	4.408
S-003	11.73	0.0	26.7	13.5	0.0340	20.8	0.369	4.41	1.58	0.36	3.364
S-014	11.73	0.0	26.7	13.5	0.0338	25.0	0.487	4.41	1.75	0.36	4.435

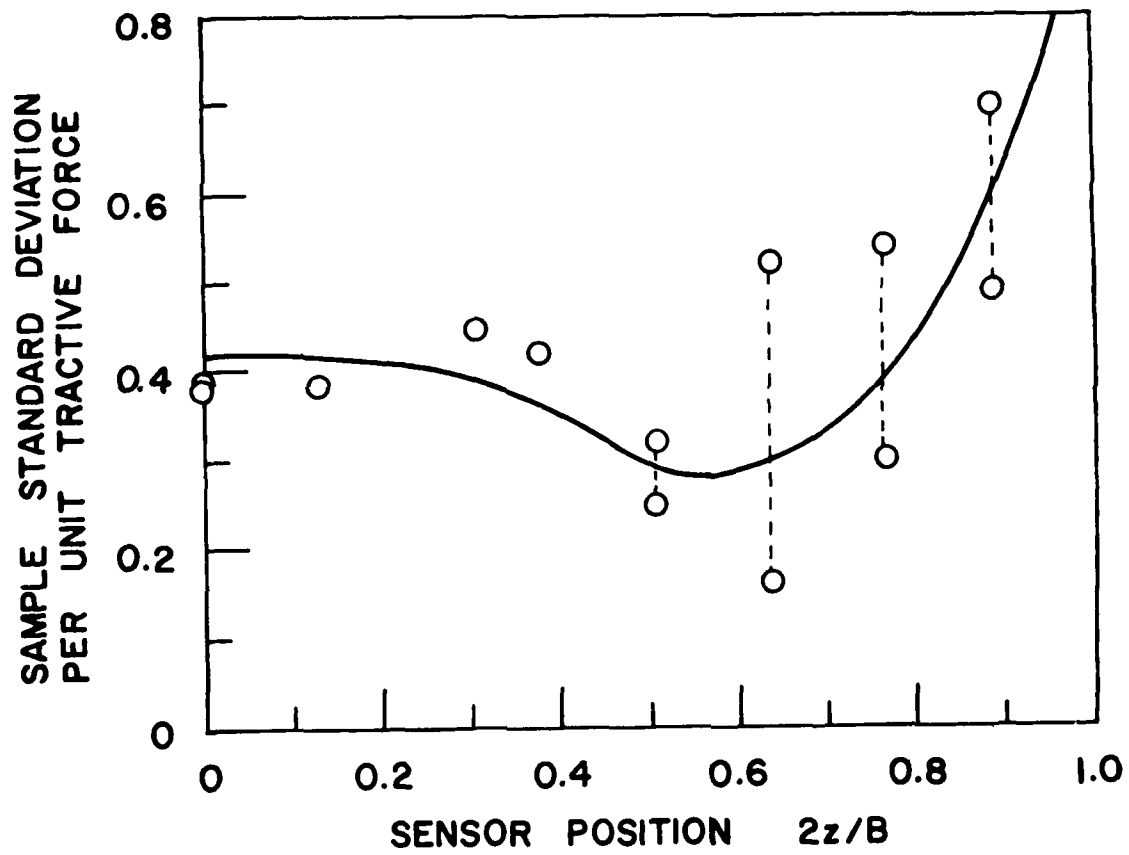


Fig. 13. The ratio $\sigma_t/\bar{\tau}_0$ plotted against $2z/B$ for channel bed measurements.

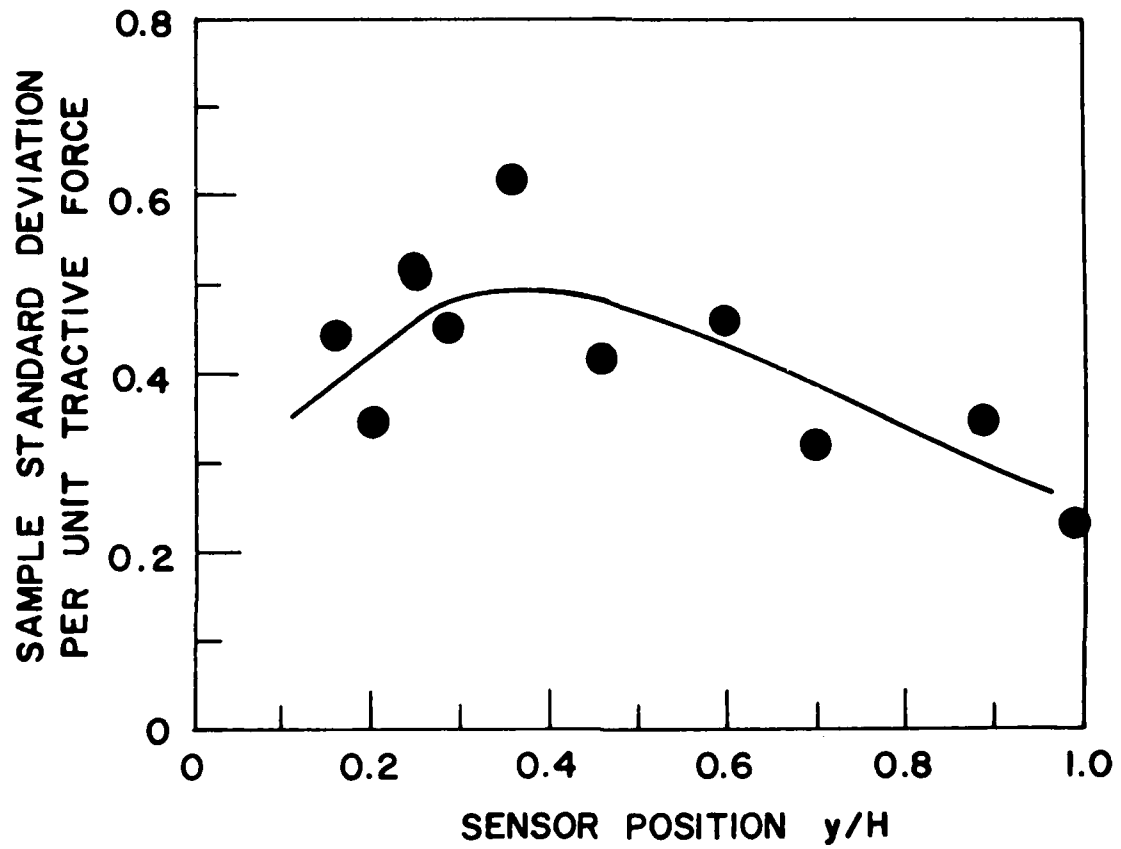


Fig. 14. The ratio $\sigma_T/\bar{\tau}_0$ plotted against y/H for channel wall measurements.

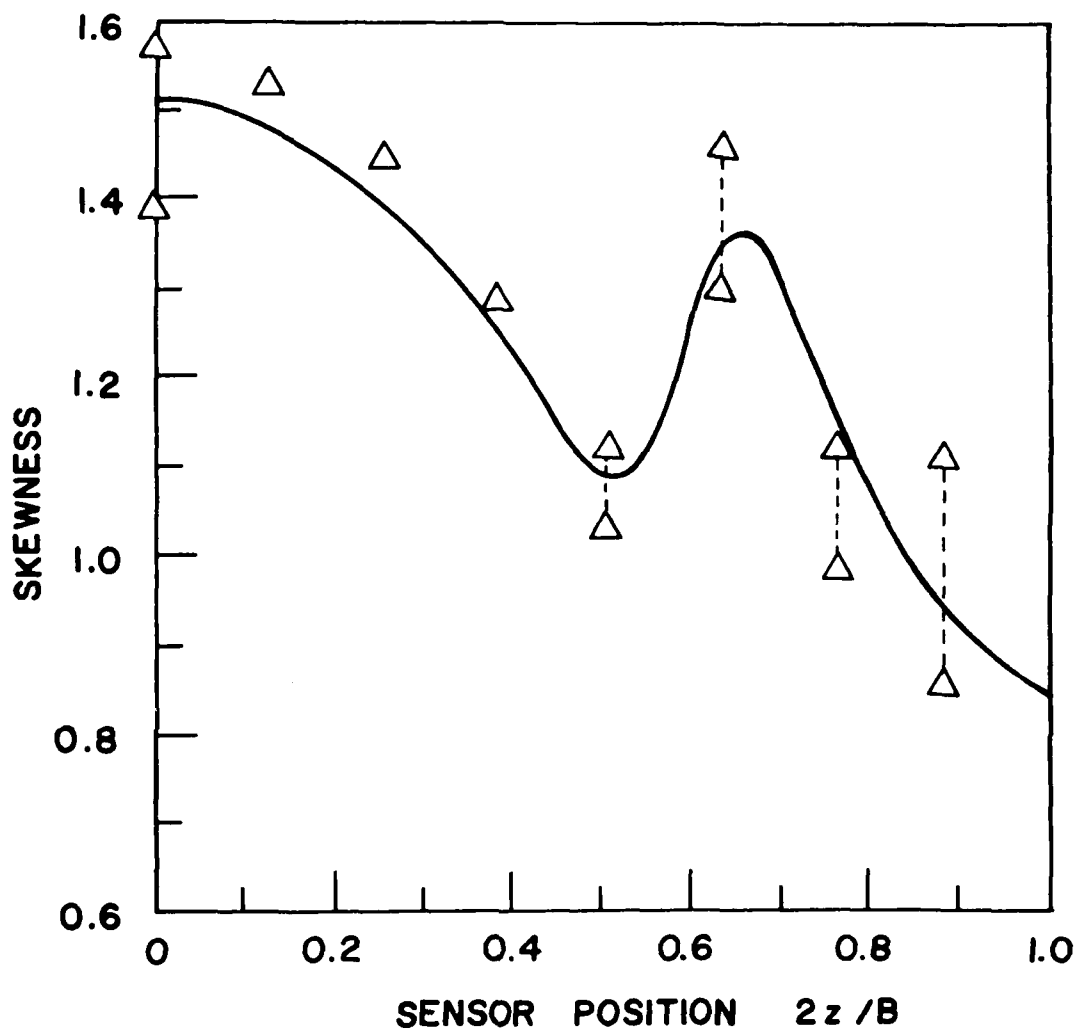


Fig. 15. The variation of shear distribution skewness across the channel bed.

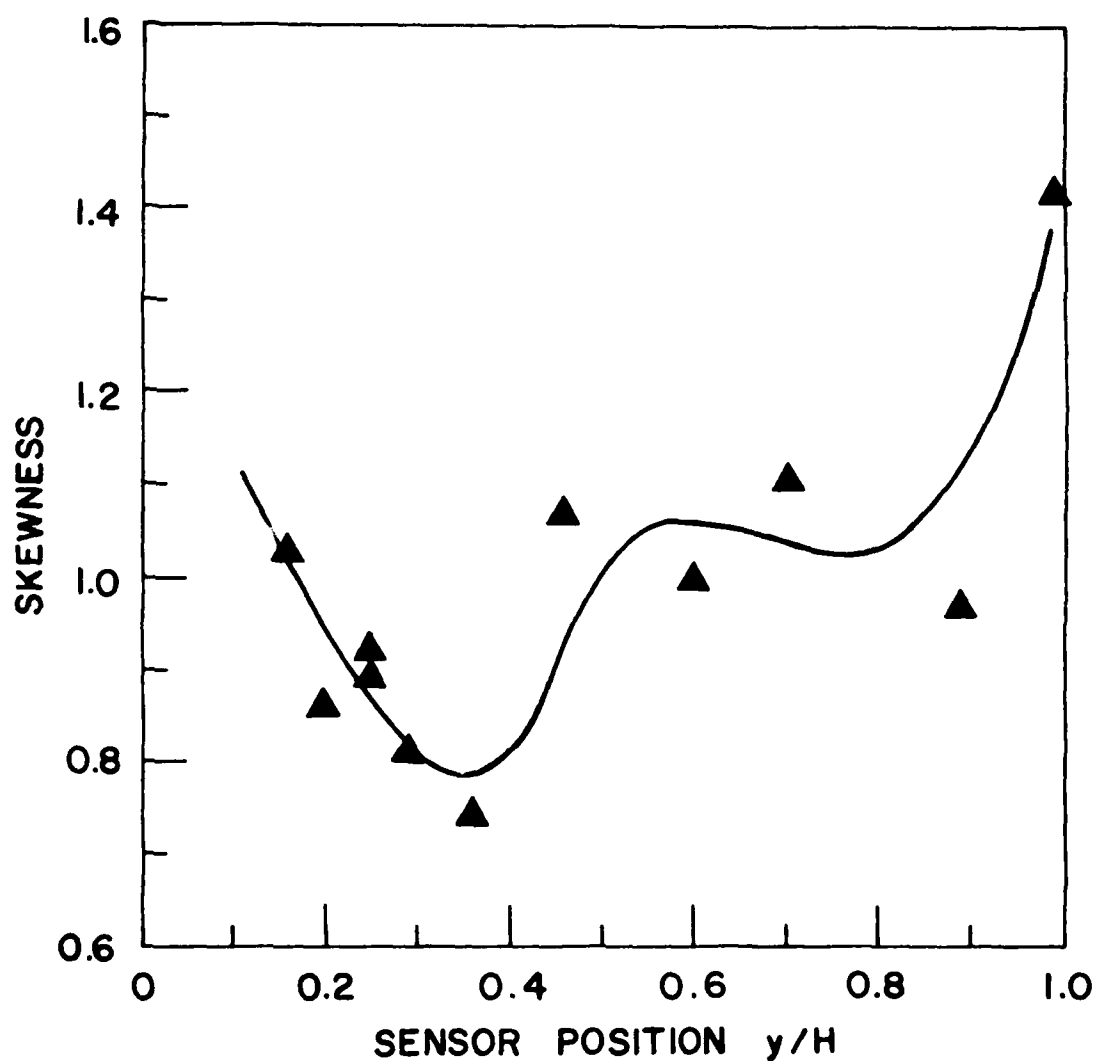


Fig. 16. The variation of shear distribution skewness up the channel wall.

Figures 17 and 18 show the variations of kurtosis along the channel bed and wall, respectively. The kurtosis is a measure of the relative peakedness or flatness of a probability distribution, and is equal to 3 for a normal distribution. Like skewness, kurtosis displays a quasiperiodic variation along the channel bed and wall. The similarity between the trends of skewness and kurtosis is marked.

The peaks and valleys exhibited by the distributions of skewness and kurtosis are believed to be real, since they were also observed by other investigators during shear flow measurements (Heidrick et. al., 1971). The scatter present in the bed data near the wall and depicted by the dashed vertical segments is quite possibly associated with flow intermittency. We found that the values of the statistical descriptors of data samples sizes ranging from 12,500 to 50,000, measured at $2z/B = 0.638$, were time dependent. This question will need to be further investigated.

3.3 PROBABILITY DENSITY ESTIMATES

Probability density estimates obtained digitally as described previously, are presented for some of the experimental runs in Figs. 19 through 24. All the probability density estimates share the following properties. (a) They are all similar in shape and cover the same approximate range of shear stress $-2 \leq \tau^* \leq 5$; (b) the estimates are clearly not Gaussian, as indicated by both the preceding figures and by the consistent positive skewness shown in Figs. 15 and 16; (c) the lower tail is bounded by an absolute value smaller than the upper tail; (d) the basic shape is a single-peak bell-shaped curve asymptotic to the axis for large values of the variate. These properties led to the hypothesis that the probability density estimates could be fitted by lognormal and/or gamma density functions. The two-parameter lognormal density function has the form:

$$p(\tau) = \frac{1}{\tau \sigma_n \sqrt{2\pi}} \exp [-(\ln \tau - \mu_n)^2 / 2\sigma_n^2], \quad 0 \leq \tau \leq \infty, \quad (21)$$

and the two-parameter gamma density function has the form:

$$p(\tau) = \frac{1}{\beta^\alpha \Gamma(\alpha)} \tau^{\alpha-1} \exp(-\tau/\beta), \quad 0 \leq \tau \leq \infty. \quad (22)$$

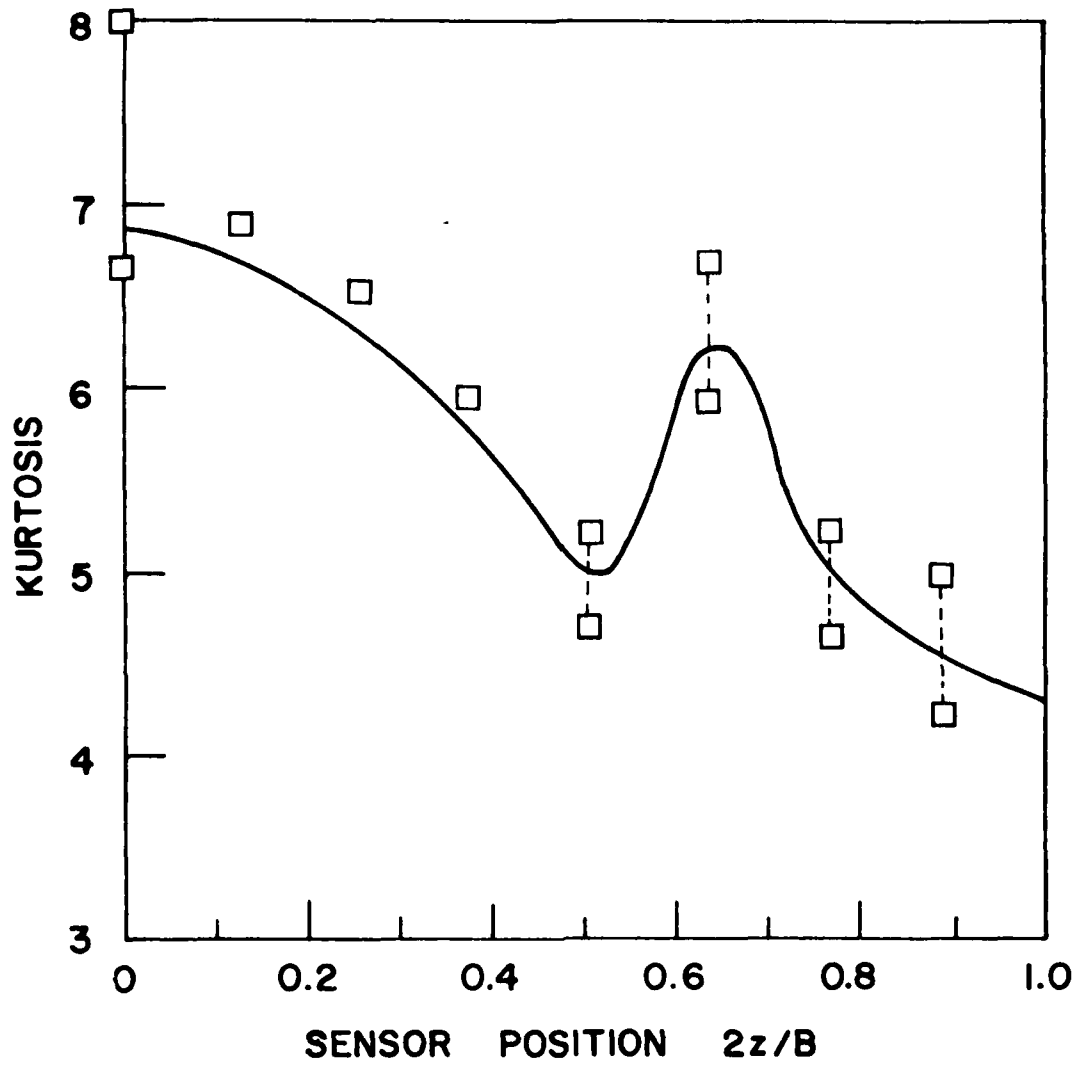


Fig. 17. The variation of shear distribution kurtosis across the channel bed.

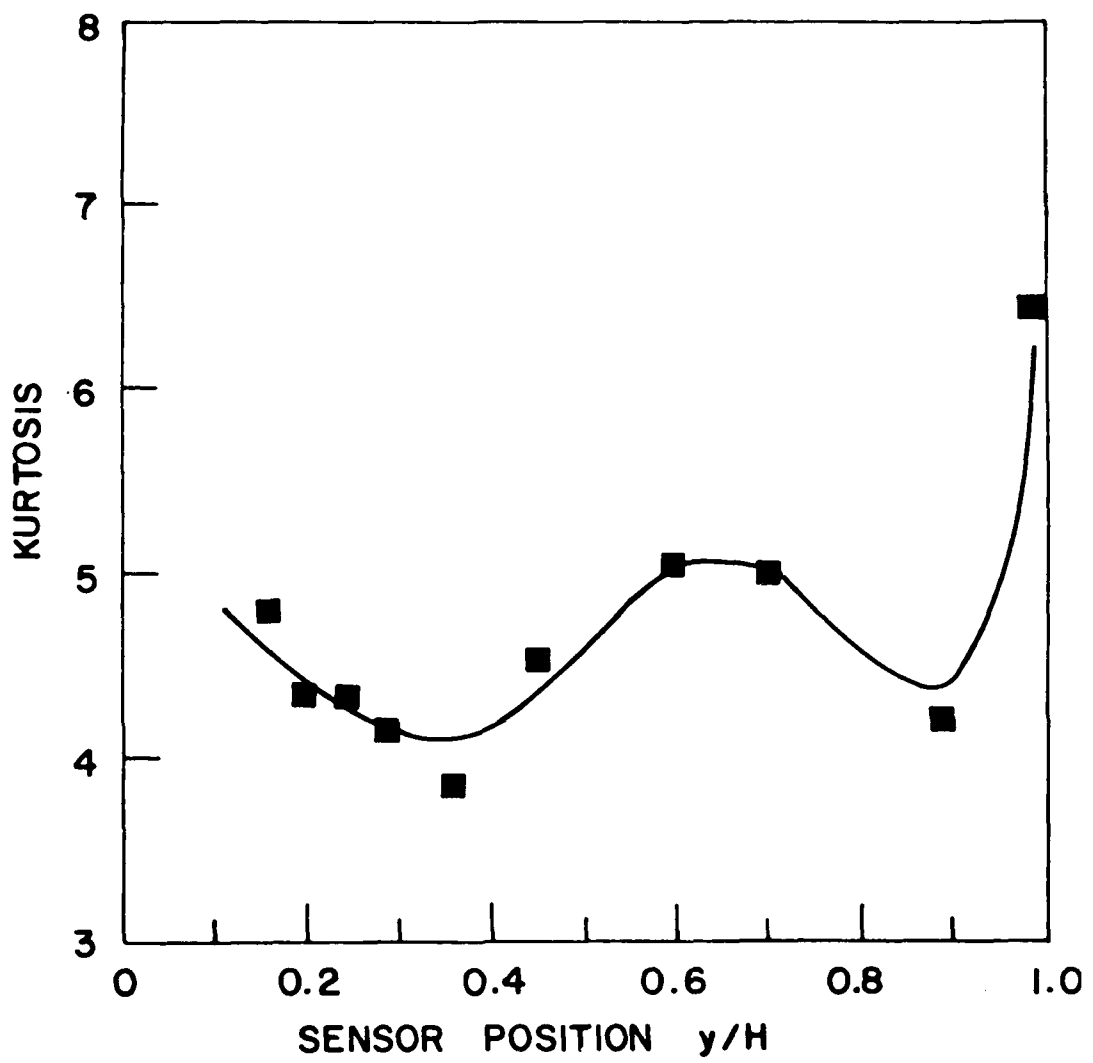


Fig. 18. The variation of shear distribution kurtosis up the channel wall.

In Eq. 22 α is a shape parameter, β is a scale parameter, and $\Gamma(\alpha)$ is the gamma function of α . Because the lognormal and gamma functions are defined in the interval $0 \leq \tau \leq \infty$, the data were transformed, before estimating the parameters, by adding the smallest value $\tau = a$ of the data range to each discrete shear stress value. This shifting of the variates simply increases the mean in the same amount but does not distort either the variance or the shape of the density functions.

The unknown parameters $\lambda_1, \lambda_2, \dots, \lambda_n$ of the theoretical density functions were evaluated by the maximum likelihood estimators. In this method, usually considered advantageous in computing parameters of skewed distributions, the parameters are obtained by maximizing the likelihood function:

$$\sum_{i=1}^n \frac{\partial}{\partial \lambda_i} [\ln p(\tau; \lambda_i)], \quad (23)$$

in which $p(\tau; \lambda_i)$ denotes the density function. This likelihood function yields n equations that can be solved for $\lambda_1, \lambda_2, \dots, \lambda_n$ in terms of the τ values. The maximum likelihood estimators obtained in this manner for the parameters appearing in Eqs. 21 and 22 are:

$$\mu_n = \frac{1}{N} \sum_{i=1}^N \ln \tau_i, \quad (24)$$

$$\sigma_n^2 = \frac{1}{N} \sum_{i=1}^N (\ln \tau_i - \mu_n)^2, \quad (25)$$

$$\alpha = \frac{1 + \sqrt{1 + (4/3)(\ln \mu - \mu_n)}}{4(\ln \mu - \mu_n)}, \quad (26)$$

$$\beta = \mu/\alpha, \quad (27)$$

$$\mu = \frac{1}{N} \sum_{i=1}^N \tau_i. \quad (28)$$

Table 2 gives the values of the parameters computed for the preceding density functions. To rate the goodness of fit of these density functions to the observed probability density estimates, the Kolmogorov-Smirnov one-sample test was used. This test is generally more powerful than the

chi-square test for goodness of fit because it is based on the maximum absolute difference between the cumulative distributions, rather than on the averaged cumulative difference. Let $F(\tau)$ define the theoretical cumulative distribution function, and $S_N(\tau)$ the sample cumulative distribution function. Then it is possible to calculate the quantity

$$D_N = \max_{\tau} |F(\tau) - S_N(\tau)| , \quad (29)$$

which is the maximum difference between the functions $F(\tau)$ and $S_N(\tau)$ over the range of τ values. Since $S_N(\tau)$ varies from sample to sample, D_N is obviously a random variable. Its distribution can be shown to be independent of $F(\tau)$. Another advantage of the D_N statistics is that it is an exact method, whereas the chi-square method requires data classification to ensure that all cell frequencies exceed five. In this case the test is no longer an exact one because the D_N values for unclassified and classified data may not be the same. Let D_N^α denote the critical value satisfying the relation

$$\text{Prob} [D_N \leq D_N^\alpha] = 1-\alpha , \quad (30)$$

where α indicates the test level of significance. Values of D_N^α are found in statistical tables for different levels of significance. When D_N exceeds D_N^α , the hypothesis that the observed sample came from a population with the specified theoretical distribution is rejected. The test statistics D_N , obtained for the distributions corresponding to Eqs. 21 and 22, are given in Table 2. Only the gamma density function fits the observed distributions within any acceptable level of significance, and then only near the corner of the channel. In the remainder of the channel perimeter neither function fits very well; however, the gamma function approaches a better fit than the lognormal function in most sensor positions.

Fig. 21 and 23 depict two density distributions measured at the bed and the wall, plotted together with the theoretical gamma distributions accepted at the 0.05 and 0.01 level of significance, respectively. In these plots the standardized theoretical distributions were computed based on the standardized variate (Eq. 19). The positive skewness displayed by the probability densities in all cases is believed to be associated with large-scale motions extending from the outer region of the flow towards the wall. The work of Grass (1971), among others, has shown that the inrush of

lumps of high momentum fluid towards the boundary is related to high positive contributions to Reynolds stresses very near the wall. In the viscous sublayer the boundary shear stress process is closely related to the local instantaneous velocity gradients induced by those Reynolds stresses.

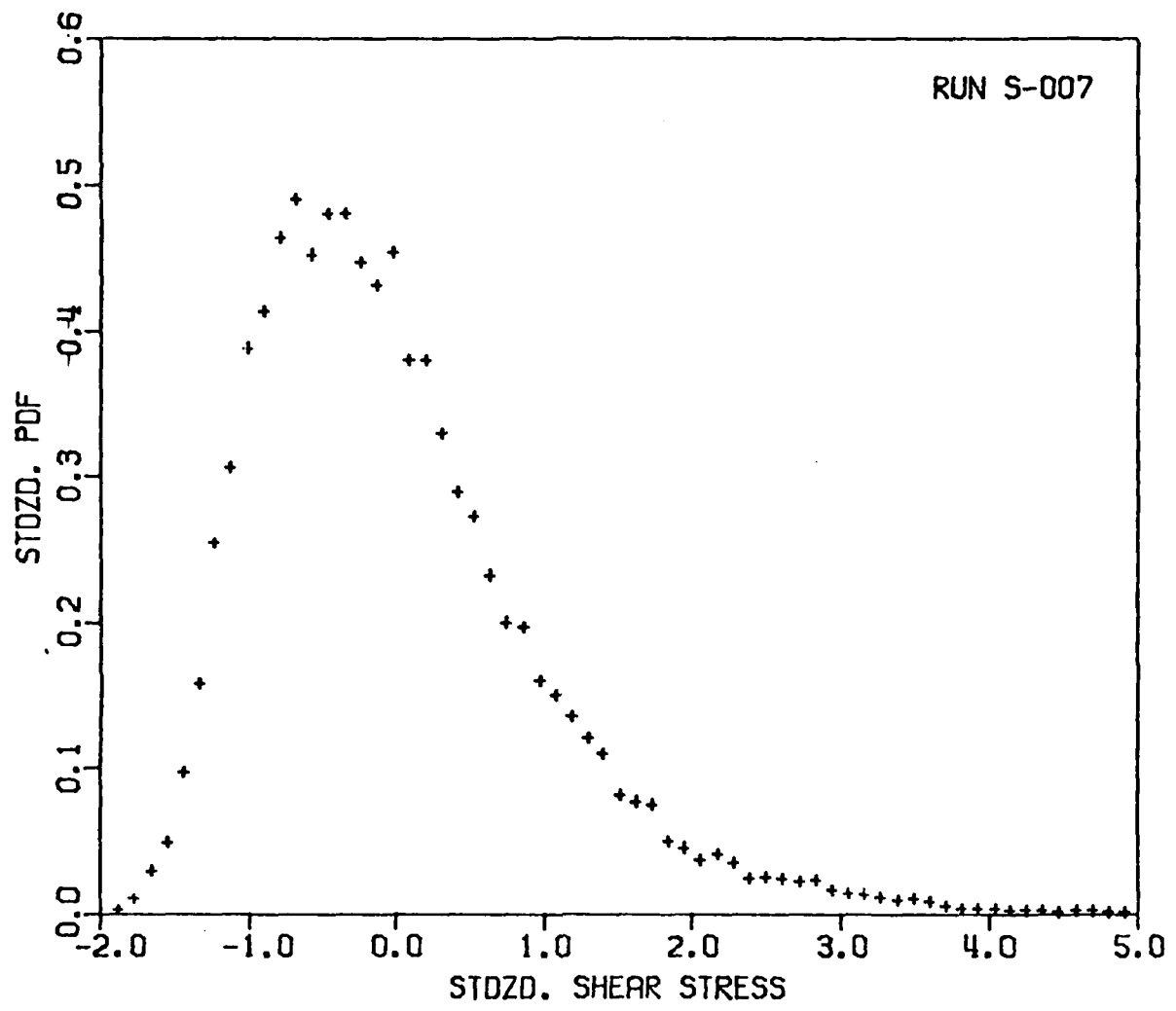


Fig. 19. Observed probability density estimates for bed shear stresses at $2z/B=0.000$ (Run S-007).

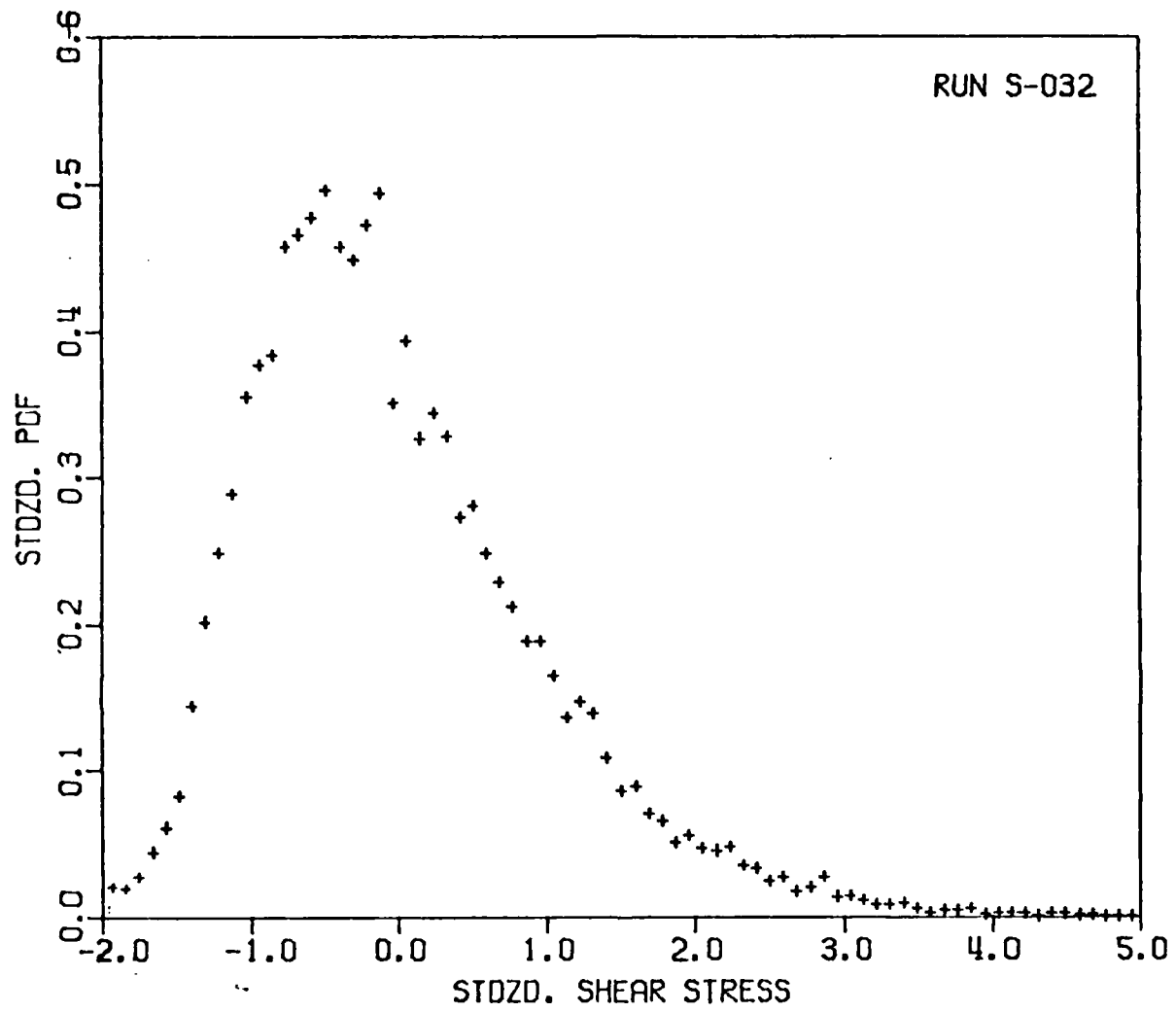


Fig. 20. Observed probability density estimated for bed shear stresses at $2z/B=0.510$ (Run S-032).

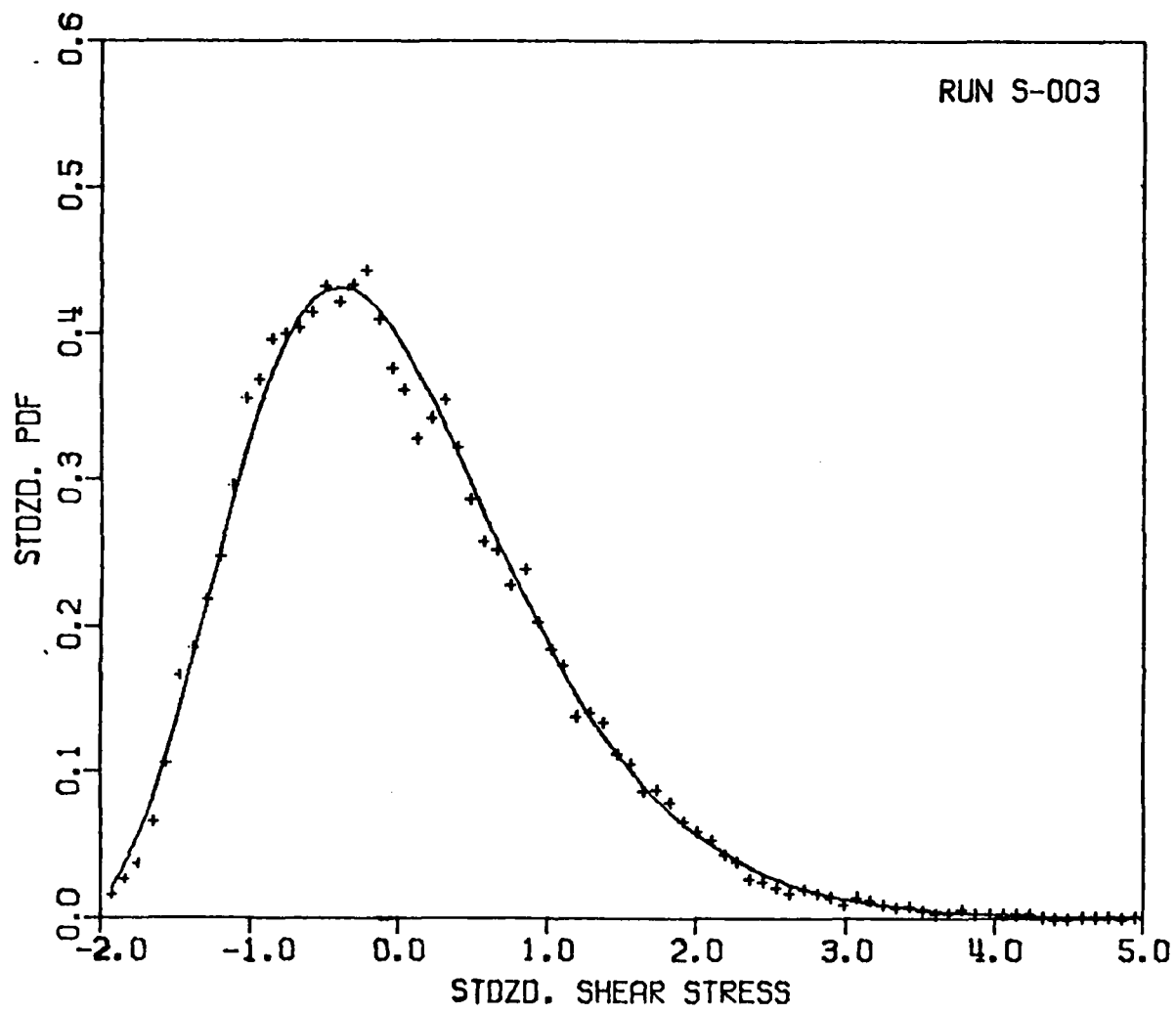


Fig. 21. Observed and theoretical gamma probability density estimates for bed shear stresses at $2z/B=0.894$ (Run S-003).

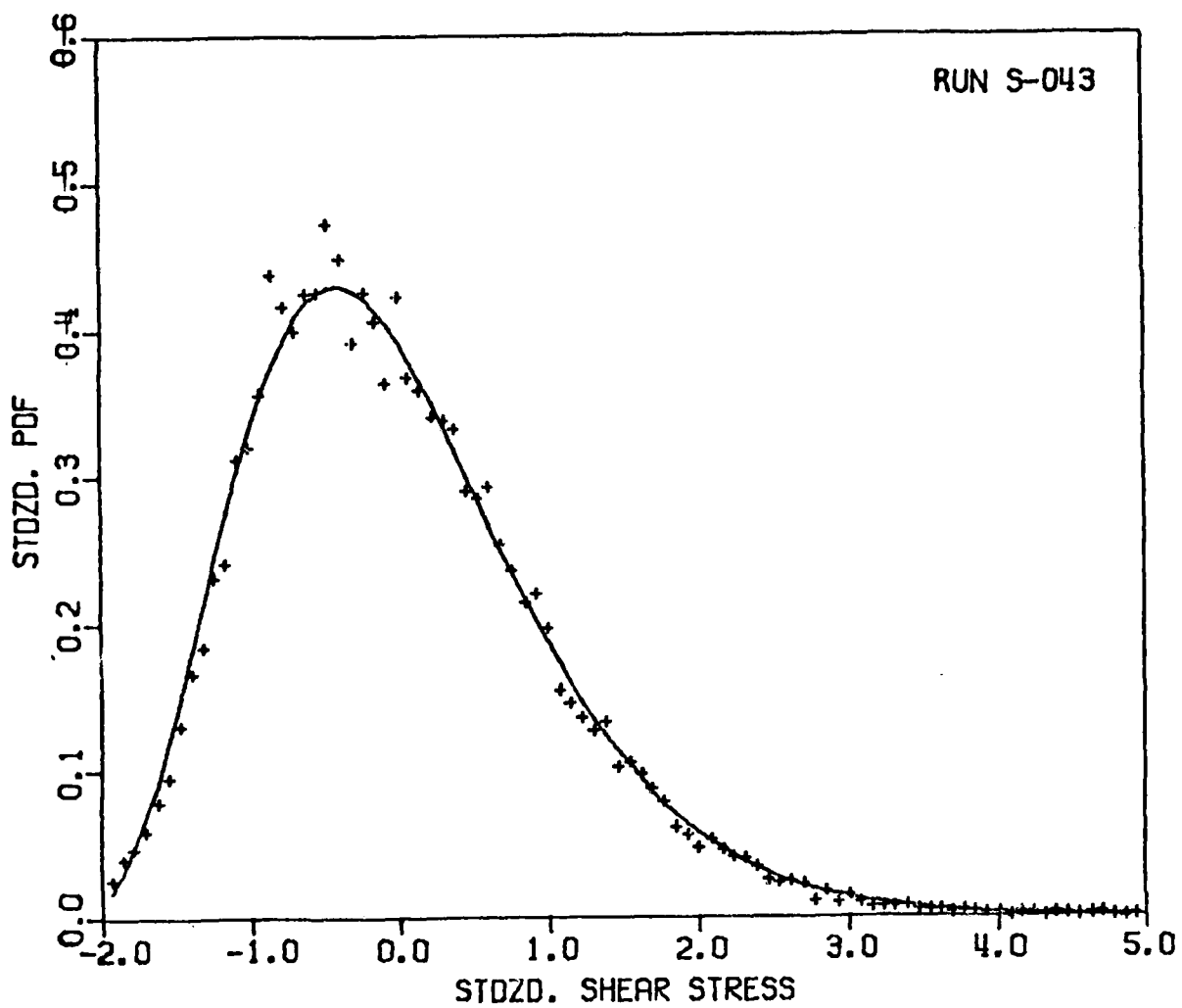


Fig. 22. Observed and theoretical gamma probability density estimates for wall shear stresses at $y/H=0.201$ (Run S-043).

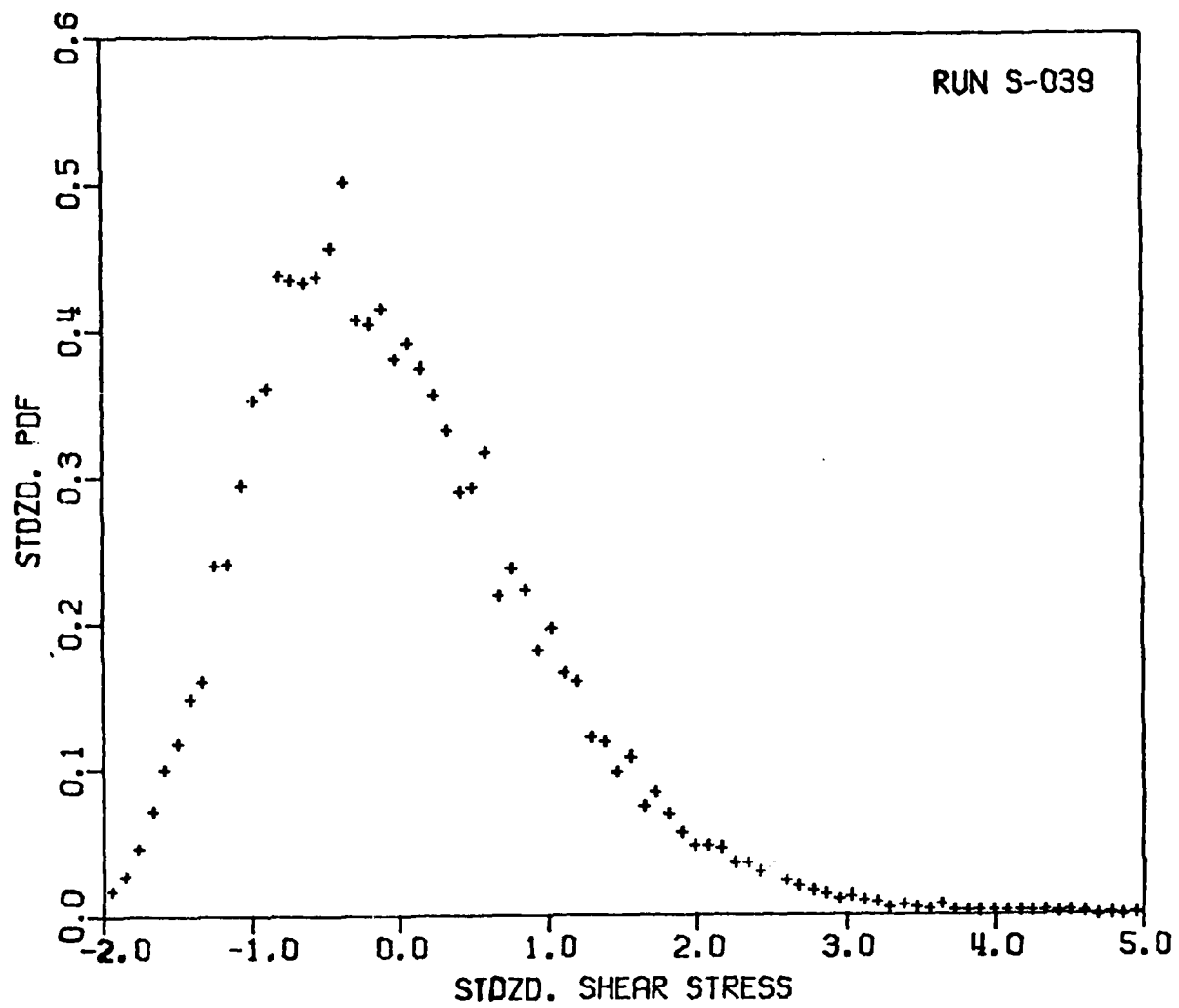


Fig. 23. Observed probability density estimates for wall shear stresses at $y/H=0.599$ (Run S-039).

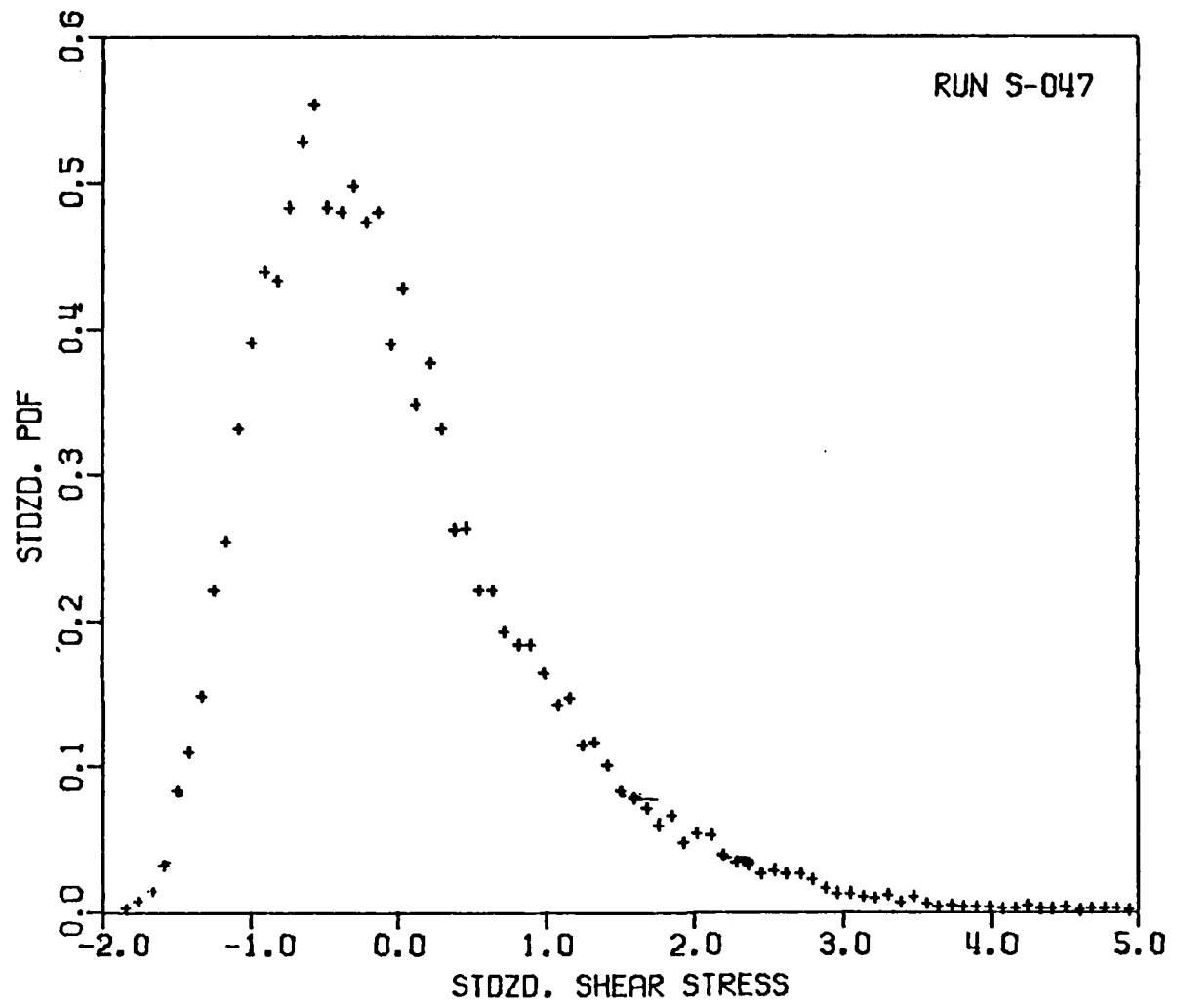


Fig. 24. Observed probability density estimates for wall shear stresses at $y/H=0.987$ (Run S-047).

Table 2. Summary of MLE parameters and Kolmogorov-Smirnov statistic

Run Number	Probe Location y/H	2z/B	Logonormal			Gamma		
			μ_n	σ_n	D_N	α	β	D_N
S-036	0.161	1.000	2.157	0.253	0.039	19.982	0.444	0.010
S-043	0.201	1.000	2.470	0.162	0.027	46.154	0.259	0.008 ^a
S-037	0.248	1.000	2.174	0.279	0.028	15.476	0.588	0.005 ^c
S-042	0.248	1.000	2.174	0.278	0.025	15.476	0.588	0.006 ^c
S-044	0.297	1.000	2.523	0.202	0.034	29.913	0.424	0.007 ^c
S-038	0.350	1.000	2.559	0.235	0.037	22.077	0.599	0.010
S-045	0.457	1.000	2.006	0.296	0.016	13.577	0.570	0.022
S-039	0.599	1.000	2.433	0.185	0.017	32.963	0.351	0.013
S-046	0.708	1.000	1.724	0.300	0.018	13.160	0.444	0.014
S-040	0.890	1.000	1.704	0.290	0.011	13.552	0.422	0.021
S-047	0.993	1.000	1.187	0.359	0.022	9.352	0.372	0.024
S-007	0.0	0.0	1.721	0.316	0.025	12.231	0.478	0.017
S-035	0.0	0.0	1.655	0.334	0.021	10.900	0.505	0.020
S-008/9	0.0	0.128	1.605	0.351	0.019	10.123	0.521	0.030
S-010	0.0	0.255	1.878	0.318	0.016	11.620	0.591	0.029
S-011	0.0	0.383	1.924	0.293	0.015	13.706	0.520	0.018
S-032	0.0	0.510	1.397	0.276	0.020	15.377	0.272	0.022
S-006	0.0	0.510	1.863	0.234	0.019	21.035	0.314	0.012
S-048	0.0	0.638	0.587	0.354	0.020	9.647	0.197	0.027
S-004	0.0	0.768	2.011	0.241	0.010	19.265	0.399	0.023
S-033	0.0	0.768	1.844	0.234	0.038	23.706	0.273	0.007 ^c
S-003	0.0	0.894	2.231	0.260	0.023	16.816	0.571	0.008 ^b
S-034	0.0	0.894	2.093	0.274	0.019	15.781	0.532	0.017

a Fit accepted at 0.01 level of significance

b Fit accepted at 0.05 level of significance

c Fit accepted at 0.10 level of significance

CONCLUSIONS AND RECOMMENDATIONS

4.1 CONCLUSIONS

This report presents recent measurements of the statistics of the instantaneous boundary shear stresses in a smooth-wall open channel flow. These measurements were made along the wetted perimeter of a channel flow with an aspect ratio of about 4.4 and a Reynolds number of about 1.7×10^5 . The results reveal the following information:

1. The wall and bed distributions of relative intensity of the shear stress fluctuations (standard deviation per unit average tractive force) follow trends similar to those exhibited by the relative local mean shear. This suggests that the mean secondary flow affects the cross-sectional distribution of relative intensity of boundary shear.
2. The coefficients of skewness and kurtosis are dependent on the transversal boundary position, differ significantly from their Gaussian limiting values, and were found to exhibit quasiperiodic variations along both bed and wall perimeters.
3. The probability density function estimates from the boundary shear stress are positively skewed, with instantaneous standardized values ranging from -2.5 to 10.00 along the bed and from -2.5 to 7.7 along the wall. The measured density functions are well fitted by the theoretical (two parameter) gamma-density distribution only near the corner. In the remainder of the channel perimeter, neither the gamma nor the lognormal functions provide a good fit, although the gamma function approaches a better fit than the lognormal in all cases. The shape of the probability density estimates are suggested to be the result of large-scale flow structures oriented towards the wall.

4.2 RECOMMENDATIONS

The measurements reported above were confined to turbulent flows over smooth beds, using sensing devices suitable only for laboratory practice. There is obviously a need for (a) extending these type of measurements to fully rough bed conditions usually encountered in the field, and (b) developing tractive-force measuring techniques appropriate for this type of environment. In order to accomplish these goals, implementation of the following experimental program is recommended:

1. Adapt a commercially available force transducer to measure instantaneous unit tractive-forces acting on discrete roughness elements.

This technique will complement that already in use for smooth beds, thus permitting direct measurement of the mean and probabilistic properties of turbulent tractive forces acting on boundaries ranging from smooth to fully rough.

2. Implement hot-film anemometry techniques for measuring the turbulent flow characteristics in the proximity of the channel bed. This will require setting up into operation existing equipment designed for the calibration of hot-film velocity sensors.
3. Investigate the relationship between the bed tractive forces and the turbulent velocity field from space cross-correlation measurements of those variables. This should be done over the entire range of bed roughnesses and for a wide variety of flow Reynolds numbers and aspect ratios. This information will permit engineers to estimate the tractive-force distributions from direct measurements of the velocity field in the proximity of the bed. Such techniques could be used by field workers to measure point tractive forces in alluvial streams where it is not possible to install any sensing device at the stream bed for direct measurement of those forces.

REFERENCES

1. Alonso, C. V., Klaus, W. H., and Wylie, K. F., "Turbulent Characteristics of Drag-Reducing Flows," Journal of Hydraulic Research, Vol. 14, No. 2, pp. 103-113, 1976.
2. Bellhouse, B. J., and Schultz, D. L., "Determination of Mean and Dynamic Skin Friction, Separation and Transition in Low-Speed Flow with Thin-Film Heated Element," J. Fluid Mech., Vol. 24, Part 2, pp. 379-400, 1966.
3. Bellhouse, B. J., and Schultz, D. L., "The Determination of Fluctuating Velocity in Air with Heated Thin-Film Gauges," Journal of Fluid Mechanics, Vol. 29, Part 2, pp. 289-295, 1967.
4. Blinco, P. H., "Spatial Structure of the Viscous Sublayer," Ph.D. Thesis, Colorado State University, Fort Collins, CO, 1974.
5. Brown, G. L., "Theory and Application of Heated Films for Skin Friction Measurements," Proceedings, Heat Transfer and Fluid Mechanics Institute, pp. 361-381, 1967.
6. Cheng, E. D. H., and Clyde, C. C., "Instantaneous Hydrodynamic Lift and Drag Forces on Large Roughness Elements in Turbulent Open Channel Flow," Sediment Symposium to honor H. A. Einstein, H. W. Shen, Ed., Colorado State Univ., Fort Collins, CO, 1971.
7. Curle, N., The Laminar Boundary Layer Equations, Oxford University Press, 1962.
8. Einstein, H. A., and El-Samni, E. A., "Hydrodynamic Forces on a Rough Wall," Rev. Mod. Phys., Vol. 21, pp. 520-524, 1949.
9. Einstein, H. A., and Li, H., "The Viscous Sublayer Along a Smooth Boundary," J. Eng. Mech. Div., ASCE, Vol. 82, pp. 945-1--945-27, 1956.
10. Grass, A. J., "Initial Instability of Fine Bed Sand," J. Hydr. Div., ASCE, Vol. 96, No. HY3, pp. 619-632, 1970.
11. Grass, A. J., "Structural Features of Turbulent Flow over Smooth and Rough Boundaries," J. Fluid Mech., Vol. 50, pp. 233-255, 1971.
12. Heidrick, T., Azad, R. S., and Banerjee, S., "Phase Velocities and Angle of Inclination for Frequency Components in Fully Developed Turbulent Flow Through Pipes," Proceedings, Second Symposium on Turbulence in Liquids, University of Missouri-Rolla, pp. 149-157, 1971.

13. Kalinske, A. A., "Turbulence and the Transport of Sand and Silt by Wind," Ann. N. Y. Acad. Sci., Vol. 44, pp. 41-54, 1943.
14. Kartha, V. C., and Leutheusser, H. J. "Distribution of Tractive Force in Open Channels," J. Hydraulics Division, ASCE, Vol. 96, No. HY7, pp. 1469-1483, 1970.
15. Melling, A., and Whitelaw, J. H., "Measurements in Turbulent Water and Two-Phase Flows by Laser Anemometry," Proceedings, Third Symposium on Turbulence in Liquids, University of Missouri-Rolla, pp. 115-134, 1973.
16. Offen, G. R., and Kline, S. J., "A Proposed Model of the Bursting Process in Turbulent Boundary Layers," J. Fluid Mech., Vol. 70, pp. 209-228, 1975.
17. Otnes, R. K., and Enochson, L., "Digital Time Series Analysis," Wiley and Sons, 1972.
18. Sutherland, A. J., "Proposed Mechanism for Sediment Entrainment by Turbulent Flows," J. Geophys. Res., Vol. 72, pp. 6183-6194, 1967.
19. Vanoni, V. A., "Measurements of Critical Shear Stress for Entraining Fine Sediments in a Boundary Layer," Calif. Inst. Tech. Rep. KH-R 7, 1964.
20. White, C. M., "The Equilibrium of Grains on the Bed of a Stream," Proc. Royal Soc. Lond., Vol. 174, pp. 322-338, 1940.
21. Wylie, K. F., Alonso, C. V., Coleman, N. L., and Darden, R., "Some Stochastic Properties of Turbulent Tractive Forces in Open-Channel flows," Proceedings, Fifth Biennial Symposium on Turbulence, University of Missouri-Rolla, pp. 181-189, 1977.